A&A, 708, A376 (2026)
https://doi.org/10.1051/0004-6361/202557108

Astronomy & Astrophysics

A $z \sim 1$ galactic-scale outflow transversally mapped to ~ 50 kpc through gravitational-arc tomography★

J. A. Hernández-Guajardo[1,★★], L. F. Barrientos[1], S. López[2], E. J. Johnston[3], C. Ledoux[4], N. Tejos[5], A. Afruni[6,7], M. Solimano[3], E. Jullo[8], H. Cortés-Muñoz[2], P. Noterdaeme[9], J. González-López[1], A. Ormazábal[1], F. Muñoz-Olivares[1], and T. A. M. Berg[10]

[1] Instituto de Astrofísica, Facultad de Física, Pontificia Universidad Católica de Chile, Av. Vicuña Mackenna 4860, 7820436 Macul, Santiago, Chile
[2] Departamento de Astronomía, Universidad de Chile, Casilla 36-D, Santiago, Chile
[3] Instituto de Estudios Astrofísicos, Facultad de Ingeniería y Ciencias, Universidad Diego Portales, Av. Ejército Libertador 441, Santiago, Chile
[4] European Southern Observatory, Alonso de Córdova 3107, Vitacura Casilla 19001, Santiago, Chile
[5] Instituto de Física, Pontificia Universidad Católica de Valparaíso, Casilla 4059 Valparaíso, Chile
[6] Dipartimento di Fisica e Astronomia, Universitá di Firenze, Via G. Sansone 1, 50019 Sesto Fiorentino, Firenze, Italy
[7] INAF – Osservatorio Astrofisico di Arcetri, Largo E. Fermi 5, Firenze I-50125, Italy
[8] Aix-Marseille Univ., CNRS, CNES, LAM, Marseille, France
[9] Institut d'Astrophysique de Paris, CNRS-SU, UMR 7095, 98bis bd Arago, 75014 Paris, France
[10] Department of Physics and Astronomy, Camosun College, 3100 Foul Bay Rd, Victoria, B.C. V8P 5J2, Canada

Received 5 September 2025 / Accepted 19 February 2026

ABSTRACT

We report spatially resolved measurements of cool gas traced by Mg II and Fe II absorption in the circumgalactic medium (CGM) of a star-forming galaxy at $z \sim 1$ (G1). The fortuitous alignment of a background gravitational arc at $z \sim 2.4$ provides seven closely spaced (∼6 kpc) transverse sightlines along the minor axis of G1, probing its CGM out to ∼50 kpc. This geometry allowed us to detect a galactic-scale outflow simultaneously in the down-the-barrel and transverse directions, where we detected blueshifted Mg II absorption lines along both types of sightlines, revealing a large-scale collimated wind. We measured blueshifted line-of-sight velocities of $v_{\rm los} \sim 62-239\,{\rm km\,s^{-1}}$ and line-of-sight velocity dispersions of $\sigma_{\rm los} \sim 53-133\,{\rm km\,s^{-1}}$, suggesting a structure dominated by bulk motion. De-projection of $v_{\rm los}$ along the minor axis indicates that the outflow material barely approaches the escape velocity and is likely to be gravitationally bound to G1. We constrained an outflow opening angle $\theta_{\rm c} \sim 18°-25°$, and a mass outflow rate of $\dot{M}_{\rm out} \gtrsim 0.06\,M_{\odot}\,{\rm yr^{-1}}$, corresponding to a mass loading factor $\eta \gtrsim 0.004$, estimated within ∼10−50 kpc (∼0.05−0.3 $R_{\rm vir}$) of the galaxy centre. Our measurements, combined with previous arc tomography data along the major axis, indicate that normalizing impact parameters by galaxy B-band luminosity substantially reduces scatter in the established anti-correlation between Mg II equivalent width and impact parameter, while also diminishing possible excess of Mg II equivalent width towards the minor axis.

Key words. galaxies: evolution – galaxies: halos – galaxies: high-redshift – intergalactic medium – quasars: absorption lines

1. Introduction

The evolution of galaxies across cosmic time is driven by processes of inflows, outflows, and re-accretion of gas, collectively known as the baryon cycle. The circumgalactic medium (CGM) serves as the interface for these processes (see reviews by Tumlinson et al. 2017; Péroux & Howk 2020; Faucher-Giguère & Oh 2023). Outflows driven by supernovae, stellar winds, and active galactic nuclei (AGN) are key for regulating star formation, distributing matter and energy, and enriching the CGM with metals. Observationally, metal-enriched outflows are nearly ubiquitous in star-forming galaxies (e.g. Weiner et al. 2009; Rubin et al. 2010; Martin et al. 2012; Rubin et al. 2014), yet it remains unclear whether and how efficiently these outflows carry baryons to the CGM or beyond (e.g. Veilleux et al. 2020; Afruni et al. 2021). Answering these questions is crucial for understanding galaxy evolution, feedback, and the missing baryon problem.

One of the most widely used tracers of cool metal-enriched gas in the CGM is the Mg II $\lambda\lambda 2796, 2803$ doublet, and is arguably one of the best tracers of the cool ($T \sim 10^4$ K) CGM (Lanzetta et al. 1991; Steidel 1995; Churchill et al. 1996; Chen et al. 2010; Bordoloi et al. 2011; Nielsen et al. 2013b; Rubin et al. 2018; Lopez et al. 2018; Dutta et al. 2020; Lundgren et al. 2021). The Mg II doublet is efficiently observable from the ground over a wide redshift range, approximately $0.1 \lesssim z \lesssim 6$, even at moderate spectral resolution (e.g. Matejek & Simcoe 2012; Nielsen et al. 2013b; Huang et al. 2021). In emission, Mg II traces resonantly scattered photons, often revealing extended halos or outflows (e.g. Rubin et al. 2011; Burchett et al. 2021; Pessa et al. 2024). In absorption, strong ($W_0 > 0.3$ Å) systems are associated with ∼100 kpc halos around star-forming galaxies (e.g. Chen et al. 2010; Bordoloi et al. 2011; Nielsen et al. 2013b) that show slow evolution with redshift (Lopez & Krogager 2025). Together, these

★ Based on observations collected at the European Southern Observatory under ESO programme 094.A-0141 (MUSE).
★★ Corresponding author: joaquin.hernandezg@uc.cl

properties establish the Mg II doublet as one of the most effective tracers for investigating the structure, kinematics, and evolution of the cool CGM throughout cosmic time.

Two complementary observational strategies have been historically used to probe gas flows in the Mg II-bearing CGM in absorption: down-the-barrel and quasar absorption lines. Down-the-barrel spectroscopy leverages the stellar continuum of the absorber galaxies themselves to probe gas along the line of sight towards the galaxy, and has revealed that outflows are ubiquitous and collimated (e.g. Rubin et al. 2014), and have velocities of $100-1000\,\mathrm{km\,s^{-1}}$ (e.g. Tremonti et al. 2007; Weiner et al. 2009; Martin & Bouché 2009; Rubin et al. 2010; Coil et al. 2011; Martin et al. 2012; Bouché et al. 2012; Rubin et al. 2014; Heckman et al. 2015; Schroetter et al. 2016). Transverse absorption-line studies against background sources – usually quasars – probe gas at much larger galactocentric distances, typically tens to hundreds of kiloparsecs, at CGM scales (e.g. Nielsen et al. 2013b; Huang et al. 2021). These reveal that Mg II absorbers are more common and stronger around blue star-forming galaxies than red quiescent ones (Chen et al. 2010), and often align with either the major or minor axis of the host galaxy (e.g. Kacprzak et al. 2012; Martin et al. 2019; Lundgren et al. 2021), a bi-modality that suggests a connection to inflows and outflows. However, both approaches have intrinsic limitations. Down-the-barrel spectroscopy allows a straightforward discrimination between inflows and outflows, but provides no information about their spatial extent. Transverse absorption, on the other hand, constrains the spatial extent of the gas through an impact parameter, but it is challenging to unambiguously associate the observed absorption kinematics with outflows, inflows, or other CGM processes.

In the era of 10m class telescopes, deep integral-field spectroscopy has opened the way for the use of extended background sources to resolve the CGM in absorption. Gravitational-arc tomography (Lopez et al. 2018) is a technique developed for studying the high-redshift CGM, leveraging bright gravitational arcs as extended background sources. This method effectively mimics many contiguous background sightlines, enabling spatially resolved spectroscopy of intervening gas associated with individual halos. Arc tomography results have shown for the first time directly that the CGM is clumpy and anisotropic (Lopez et al. 2018), and have revealed the presence of extended co-rotating discs (Lopez et al. 2020; Tejos et al. 2021) and signatures of outflows (Tejos et al. 2021; Mortensen et al. 2021; Fernandez-Figueroa et al. 2022; Shaban et al. 2025). Furthermore, the contiguous spatial information uniquely provided by arc tomography data has also placed constraints on the kiloparsec-scale structure of the cool and warm CGM (Afruni et al. 2023; Lopez et al. 2024; Shaban et al. 2025). This rich spatial information offers a unique window to probe the structure and propagation of metal-enriched flows at CGM scales.

In this work we present gravitational-arc tomography along the projected minor axis of an intervening galaxy at $z \sim 1$, traced simultaneously by down-the-barrel and transverse absorption. This configuration arises from the fortuitous alignment between a bright background gravitational arc and a foreground star-forming galaxy at $z \sim 1$. It enables us to probe the possible outflowing gas both against the galaxy itself and, critically, along its minor axis – where outflows are expected to be most prominent and evident – over seven nearly contiguous sightlines spanning a ∼50 kpc projected line.

Our paper is organized as follows. In Sect. 2 we describe the observations. In Sect. 3 we describe the construction of the lens model of the foreground galaxy cluster. In Sect. 4 we present the emission properties of the absorbing galaxy, based on HST imaging and MUSE spectroscopy. The absorption strength and kinematic measurements of the intervening gas are described in Sect. 5. Our main results are presented in Sect. 6 and discussed in Sect. 7. Throughout this paper we assume a Lambda cold dark matter cosmology with the following parameters: $H_0 = 70\,\mathrm{km\,s^{-1}\,Mpc^{-1}}$, $\Omega_\mathrm{m} = 0.3$, and $\Omega_\Lambda = 0.7$. Magnitudes are reported in the AB system.

2. Observations

RCS 0224-0002 is a galaxy cluster at $z_\mathrm{cluster} = 0.773$ discovered by the Red Cluster Sequence Survey (Gladders et al. 2002). The cluster acts as a gravitational lens for two background galaxies observed as extended and bright gravitational arcs at $z_A = 4.877$ and $z_B = 2.395$ (Gladders et al. 2002; Swinbank et al. 2007; Smit et al. 2017), hereafter referred to as "arc A" and "arc B", respectively, and shown in Fig. 1. A star-forming galaxy at $z \approx 0.987$ (G1 from now on) is foreground and close in projection to arc B (see Fig. 1). Absorption features of Mg II and Fe II are detected at the redshift of G1 in the spectrum of arc B, which we interpret as cool CGM gas associated with G1, assuming the galaxy is isolated.

2.1. HST imaging

We used archival *Hubble* Space Telescope (HST) imaging available in the Mikulski Archive for Space Telescopes (MAST), obtained under programmes GO 14497 (PI: Smit) and GO 9135 (PI: Gladders). The system was observed with the Wide Field Planetary Camera 2 (WFPC2) in F606W (6×1.1 ks), the Advanced Camera for Surveys (ACS) in F814W (12×1.1 ks), and the Wide Field Camera 3 (WFC3) in F125W and F160W (each 2.6 ks). All images were reduced using DrizzlePac (Anand et al. 2025), resampled onto a common $0.03''\,\mathrm{pix^{-1}}$ grid. A colour composite image using the F160W, F125W, and F814W filters is shown in Fig. 1.

2.2. MUSE spectroscopy

In this paper, we used archival integral-field spectroscopy from VLT/MUSE (Programme 094.A-0141, PI: Swinbank; Bacon et al. 2010), observed between UT November 13, 2014, and September 16, 2016. We used the ESO MUSE pipeline (Weilbacher et al. 2012) in the ESO Recipe Execution Tool (EsoRex v2.8.3) environment (ESO Cpl Development Team 2015) to reduce the data. As part of this routine, we created master bias, flat-field, and vacuum wavelength calibrations for each night using the associated raw calibrations provided by the Archive Facility. These master calibrations were applied to the raw science and standard-star observations as part of the pre-processing steps.

The reduced standard-star observations were used to create a flux calibration solution for each night, which was applied to the science frames. The sky background was directly measured and subtracted from the individual science frames using spaxels identified as representing the sky. The flux-calibrated and sky-subtracted exposures were then combined to produce a single data cube. The residual sky contamination was removed using the Zurich Atmosphere Purge (ZAP, Soto et al. 2016) code. The final combined cube has a total exposure time of 3.75 h with an average point spread function (PSF) full width at half

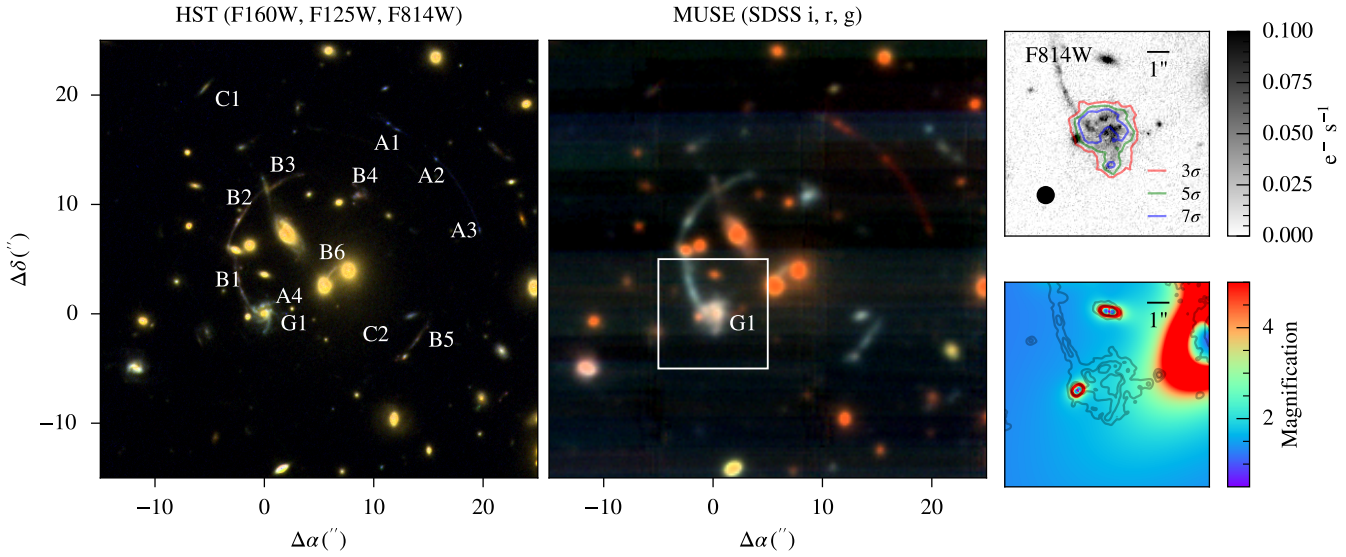

Fig. 1. *Left*: HST RGB (F160W, F125W, and F814W) image centred on the lensing cluster RCS 0224-0002. The labels indicate the positions of G1 and the lensed sources reported by Smit et al. (2017) used to constrain the lens model. The redshifts of the lensed galaxies A, B, and C are 4.877, 2.395, and 5.498, respectively. *Centre*: MUSE RGB image constructed by convolving the cube with the transmission curves of the broad-band SDSS *i*, *r*, *g* filters. The white square, centred on G1, shows the size of the rightmost panels. *Top right*: HST/F814W cutout centred on G1. The red, green, and blue contours show the 3σ, 5σ, and 7σ levels where its [O II] emission is detected in the MUSE data. The typical PSF FWHM of 0.8″ of the MUSE observations is represented by the diameter of the solid black circle. *Bottom right*: magnification map centred on G1 showing the differential lensing effect at the redshift of G1. The overlaid HST/F814W contours delineate the distribution of light from the surrounding sources. Sources enclosing areas of higher magnification correspond to cluster member galaxies.

maximum (FWHM) of ≈0.8″ at ∼5500 Å and a 1σ sensitivity of 1.6×10^{-20} erg s^{-1} cm^{-2} Å^{-1} at ∼5500 Å.

3. Strong lensing model

We constructed a strong lensing model of the foreground galaxy cluster to recover intrinsic spatial scales and physical properties in the absorber plane (i.e. at the redshift of G1). We guided the construction of our lens model by the one presented by Smit et al. (2017). The model was constrained using the positions and redshifts of multiple lensed sources identified in HST imaging and MUSE spectroscopy, including arcs A, B, and C, which are shown in Fig. 1. The redshifts of arc A ($z_A = z_{[\mathrm{O\,II}]} = 4.8760$) and arc B ($z_B = z_{\mathrm{C\,III]}} = 2.396$) were measured from the nebular [O II] and C III] emission lines, respectively, by Smit et al. (2017), in their MUSE observations, in which they also performed a blind survey of Lyα emitters, identifying the lensed source C with $z_C = z_{\mathrm{Ly}\alpha} = 5.498$.

The details of the strong lens modelling are presented in Appendix A. Our best-fit model achieves an image-plane RMS of 0.79″, with a $\chi^2 = 13.7$ with 11 free parameters. We use this model to reconstruct the geometry in the absorber-plane and to correct the observed fluxes for lensing magnification. Due to its proximity along the line of sight to the lensing galaxy cluster, G1 is subject to small (but non-negligible) distortion and magnification from the strong lensing effect. In Fig. 1 we show the magnification map around G1, from which we measured an average magnification factor of $\mu = 1.89 \pm 0.07$ (areal average within the 3σ contour of the [O II] emission, shown in Fig. 1), a value that is robust to the specific lens model parametrization chosen for the analysis. For reconstructing the absorber-plane geometry, we applied the deflection matrices to the image-plane (i.e. as observed) positions, through the lens equation (see e.g. Lopez et al. 2018). Impact parameters (ρ) are defined as the absorber-plane projected distances to the centre of G1. By sampling the deflection matrices from the posterior distributions of the model parameters, we estimated a 1σ confidence interval of the deflections, which propagates into an uncertainty of 0.5 kpc on ρ in the absorber plane. Following Lopez et al. (2020), we arbitrarily adopted a total uncertainty of 1.5 kpc on the impact parameters, corresponding to half of the binned spaxel size in the absorber plane (see Sect. 5) to account for systematics (astrometry and lens model degeneracies).

4. G1 properties

This section details the photometric, kinematic, and stellar population properties of G1, which are summarised in Table 1.

4.1. Photometry and morphology

We performed aperture photometry on the HST imaging using `SExtractor` (Bertin & Arnouts 1996). The measured fluxes were corrected for lensing magnification by dividing the integrated fluxes by the average magnification and corrected for Galactic extinction using the recalibration from Schlafly & Finkbeiner (2011) to the dust extinction maps from Schlegel et al. (1998), assuming an F99 (Fitzpatrick 1999) dust extinction law. The rest-frame *B*-band luminosity was estimated from the HST F814W band, which approximately corresponds to the B-band at $z \sim 1$. We assumed a characteristic rest-frame B-band absolute magnitude $M_B^\star = -21.416$ at $z \sim 1$ by interpolating the B-band luminosity function from Willmer et al. (2006). We find that G1 has a luminosity of $L_B = 2.6\ L_B^*$, above the characteristic luminosity at $z \sim 1$.

We used `GALFIT` (Peng et al. 2002) on the de-lensed F814W data to analyse the rest-frame *B*-band flux profile of G1 by fitting a single Sérsic component with all parameters free. The

best-fit Sérsic index is $n \approx 1.2 \pm 0.2$, consistent with an exponential disc profile. We estimated the inclination angle from the axis ratio q, assuming an infinitely thin disc ($\cos i = q$). The Sérsic index, axis ratio, position angle (PA), and effective radius (R_e) are listed in Table 1, while the best-fit model and residuals are shown in Fig. 2. The residuals reveal spiral features and compact star-forming clumps, indicative of a clumpy, gas-rich disc. Such structures are typical of high-redshift discs undergoing active star formation (Elmegreen et al. 2005; Law et al. 2007; Förster Schreiber et al. 2009; Guo et al. 2015; Shibuya et al. 2016; Kalita et al. 2025).

4.2. Stellar and halo properties

We used BAGPIPES (Carnall et al. 2018, 2019) to model the spectral energy distribution (SED) of G1 by jointly fitting its MUSE and HST photometry. The resulting stellar mass, star formation rate (SFR), and their uncertainties were inferred from the posterior distributions. We also estimated the SFR independently from the [O II] luminosity using the Kennicutt (1998) calibration. Both SFR estimates agree within 1σ and are listed in Table 1. With a specific SFR of $7.58 \times 10^{-10}\,\mathrm{yr}^{-1}$, G1 lies in the star-forming main sequence at $z \sim 1$ (Popesso et al. 2023).

Next, from the inferred stellar mass, we estimated a total halo mass M_h using the stellar-mass-halo-mass (SMHM) relation from Moster et al. (2010). Finally, we estimated the virial radius (R_vir), maximum circular velocity (V_circ), escape velocities ($V_\mathrm{esc}(r)$), and dark matter (DM) halo velocity dispersion (σ_DM). All these properties are listed in Table 1 and the details of the methodology are described in Appendix B.

4.3. Morpho-kinematic modelling

As shown in Fig. 1 (top right), the [O II] emission of G1 extends over $\sim 2''$ and is therefore spatially resolved in the MUSE data, given the average PSF FWHM of $\sim 0.8''$. We do not detect extended [O II] emission beyond the stellar disc, which is expected from the exponential decrease in the surface brightness profile of ionized gas emission (e.g. Nielsen et al. 2024). Given the spectral resolution of MUSE (FWHM of $\sim 50\,\mathrm{km\,s}^{-1}$ at the rest-frame of G1 at $z \sim 1$), we are able to resolve the [O II] doublet and recover spatially resolved kinematics, as shown in the [O II] centroid-velocity map in Fig. 3. The [O II] velocity field clearly resembles a typical rotating disc (e.g. Guérou et al. 2017; Patrício et al. 2018).

We modelled the disc kinematics of G1 in the absorber plane using GalPak^{3D} (Bouché et al. 2015). We first de-lensed the MUSE data by applying the deflections from the lens model, reconstructing the absorber-plane emission on a regular grid with the native MUSE spaxel size of $0.2''$, following the method described in Tejos et al. (2021). We assumed an arctan rotation curve for the [O II] kinematics and an exponential surface brightness profile. The best-fit model parameters: systemic redshift ($z_{[\mathrm{O\,II}]}$), maximum rotation velocity (v_max), turnover radius (r_to), effective radius (R_e), intrinsic gas velocity dispersion (σ_gas), inclination (i), and position angle (PA) are listed in Table 1. Hereafter, we adopt $z_{[\mathrm{O\,II}]}$ as the systemic redshift of G1 ($z_\mathrm{G1} = z_{[\mathrm{O\,II}]}$).

The best-fit PA and R_e of the [O II] emission agree with those obtained from GALFIT within 2σ. We use the GalPak^{3D} PA to define the kinematic major and minor axes of G1, shown in Figs. 3 and 4. However, the i derived from GalPak^{3D} (65.5°) differs by ~50% from that inferred via the axis ratio (42.3°). Since the kinematic model incorporates both morphological and kinematic constraints, it provides a more reliable estimate of the inclination; thus we adopt the GalPak^{3D}–derived i as the fiducial value.

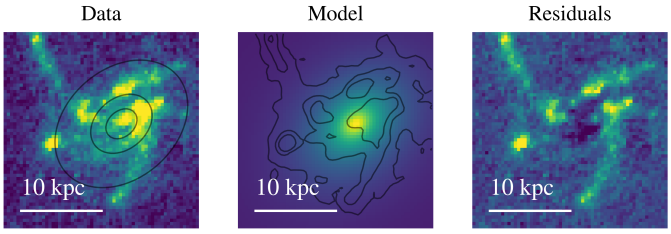

Fig. 2. *Left*: de-lensed F814W cutout centred on G1. The black contours show representative flux levels of the best-fit Sérsic model. *Centre*: best-fit single-component Sérsic model obtained with GALFIT. The black contours indicate the same flux levels as in the left panel. Best-fit R_e, PA, q, and n values are listed in Table 1. *Right*: flux residuals from the best-fit model.

The r_to is unusually small, likely because the [O II] emission is weaker in the central regions of G1 and dominated by the star-forming clumps (Fig. 1), limiting the sensitivity of the model to the inner velocity gradient. As a result, the modelling of the inner velocity structure may be more uncertain. Nevertheless, the large-scale kinematic parameters (v_max, PA, and i) remain robust, as they are primarily constrained by the outer regions with stronger [O II] emission. In the case of σ_gas, the small value of $\sim 10\,\mathrm{km\,s}^{-1}$ is consistent with expectations for cool ionized gas in star-forming discs.

Altogether, the morphological, kinematic, and stellar population properties of G1 point to a typical main-sequence disc galaxy at $z \sim 1$, unperturbed by major interactions, undergoing sustained star formation. We do not find any companion galaxy within $3000\,\mathrm{km\,s}^{-1}$ of z_G1 in the MUSE field of view ($\sim 500\,\mathrm{kpc} \times 500\,\mathrm{kpc}$ at z_G1), and thus we assume that G1 is an isolated galaxy. These properties provide essential context for interpreting the intervening metal absorption lines.

5. Intervening absorption properties

Intervening Mg II $\lambda\lambda$2796, 2803 and Fe II $\lambda\lambda$2586, 2600 absorption lines at $z_\mathrm{abs} \sim z_\mathrm{G1}$ are detected over the B1 and B2 images of arc B, and over G1. To measure the absorption line properties, we apply 4×4 spatial binning to the native $0.2''$ MUSE spaxels, following Lopez et al. (2018). This yields binned spaxels of $0.8''$, spaced by at least one PSF FWHM, balancing the need to boost S/N and minimize spaxel crosstalk, while preserving sufficient spatial resolution to map the intervening absorption lines. We define a mask enclosing G1, and the B1–B6 arc images, and retain only those binned spaxels with continuum S/N ≥ 2 around the Mg II spectral region for the subsequent analysis.

We fit the combined Mg II and Fe II absorption spectrum using four Gaussian components, one per transition. The velocity centroid and dispersion were tied for all four lines, under the assumption that they trace gas with similar properties (e.g. Churchill & Vogt 2001). For each ion, the relative amplitudes of the two transitions were allowed to vary between the optically thin limit (set by the ratio of their oscillator strengths) and the optically thick limit (unity ratio). With $R \sim 2000$ at 5500 Å, MUSE lacks the spectral resolution to de-blend individual narrow kinematic components; hence, each transition is modelled with a single Gaussian component. The line-of-sight velocity (v_los) and velocity dispersion (σ_los) are then derived from the

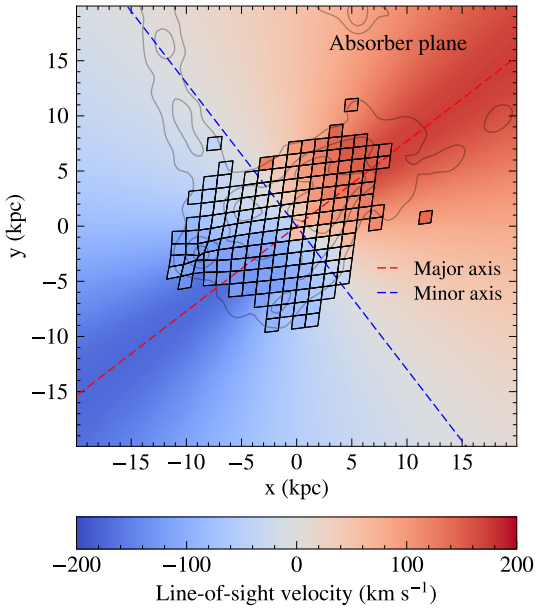

Fig. 3. De-lensed (absorber-plane) centroid-velocity map of the [O II] emission from G1 and ERD model kinematics. Zero velocity is defined at z_{G1}. Open rhomboids indicate native MUSE spaxels mapped into the absorber plane, with colours representing the measured line-of-sight [O II] velocity centroid. The background colourmap shows the line-of-sight velocity field from the best-fit arctan disc model obtained with GalPak^{3D}. The dashed lines mark the kinematics major (red) and minor (blue) axes of G1. The grey contours trace the HST/F814W flux distribution. The spaxel-based velocities are shown for illustrative purposes only: GalPak^{3D} does not extract velocities per spaxel, but fits a synthetic data cube convolved with the instrumental LSF and PSF, which is directly compared to the observed cube.

Gaussian centroid and width, respectively, with the latter corrected for instrumental broadening by subtracting the instrumental line spread function (LSF) in quadrature. Rest-frame equivalent widths ($W_r = \sqrt{2\pi}A\sigma/(1+z_{abs})$) were calculated in the continuum-normalised spectrum from the Gaussian parameters σ and A (standard deviation and amplitude, respectively) in the rest-frame of G1. The continuum level was independently measured for each transition on 100 Å windows on both the blue and red sides of the absorption features. The 1σ uncertainties in W_r (σ_{W_r}) were derived through the propagation of the uncertainties in A and σ.

We define a significant detection as having a rest-frame equivalent width significance $W_r/\sigma_{W_r} \geq 2$ in at least two transitions. For spaxels meeting the S/N but lacking significant detections, we report 2σ upper limits: $2\sigma_{W_r}$, where $\sigma_{W_r}(1+z_{abs}) = \mathrm{FWHM}/\langle \mathrm{S/N} \rangle$, following Lopez et al. (2018). We detect significant absorption on seven transverse and 13 down-the-barrel sightlines. While the rather loose S/N pre-selection (S/N $\geq$ 2) ensured scanning of all arc spaxels, the final classification of detections is automated and based on the above significance criterion. In Figs. F.1 and G.1 we show the image-plane binned spaxels and their fitted Gaussian profiles (when S/N $\geq$ 2), for Mg II and Fe II, respectively. Only spaxels in arcs B1, B2, and over G1 show significant absorptions. The derived v_{los} values are measured with respect to z_{G1}, and span a range of $\approx [-60, -240]$ km s^{-1} across all sightlines.

Absorber-plane impact parameters ρ and azimuthal angles ϕ are defined relative to the de-lensed centroid and receding major axis of G1, respectively, following Tejos et al. (2021). Table E.1 details the absorption properties measured on each spaxel. The image-plane distribution of spaxels with detected absorption lines, and the absorber-plane distribution of $W_r(2796)$, v_{los}, and σ_{los}, for Mg II λ2796, are shown in Fig. 4. These spatially resolved absorption maps serve as the basis for our results presented in the following section.

Table 1. G1 properties.

Magnification	$\mu = 1.89 \pm 0.07$
From [O II] emission and broad-band imaging (see Sect. 4)	
Right Ascension	RA = 02h24m34.10s
Declination	Dec = −00d02m30.9s
Effective radius (Stars) [a,e]	$R_e = 8.1 \pm 1.2$ kpc
Position angle (Stars) [a,e]	PA = 130.7 ± 2.3°
Axis ratio (Stars) [a,e]	$q = 0.739 \pm 0.015$
Inclination (Stars) [a,e,f]	$i = 42.3 \pm 1.3°$
Sérsic index (Stars) [a,e]	$n = 1.2 \pm 0.2$
Apparent magnitude (F814W) [b,e]	$m_B = 20.97 \pm 0.16$
Absolute magnitude (∼B band) [b,e]	$M_B = -22.47 \pm 0.16$
Luminosity (∼B band) [b,e]	$L_B = 2.6 \pm 0.4\ L_B^\star$
Stellar mass [b]	$\log(M_\star/M_\odot) = 10.29 \pm 0.01$
SFR from SED [b]	$\mathrm{SFR_{SED}} = 15.05 \pm 0.27\ \mathrm{M_\odot\ yr^{-1}}$
SFR from [O II] [b,c]	$\mathrm{SFR_{[O\ II]}} = 15 \pm 4\ \mathrm{M_\odot\ yr^{-1}}$
Specific SFR [b]	$\mathrm{sSFR_{SED}} = (7.58 \pm 0.29) \times 10^{-10}\ \mathrm{yr^{-1}}$
[O II] Luminosity [b]	$L_{[O\ II]} = (9.45 \pm 0.05) \times 10^{41}$ erg s^{-1}
From morpho-kinematical analysis of [O II] emission (see Sect. 4.3)	
Systemic redshift	$z_{G1} = z_{[O\ II]} = 0.986790 \pm (4 \times 10^{-6})$
Maximum rotation velocity (Gas)	$v_{max} = 191 \pm 2$ km s^{-1}
Turnover radius (gas) [a]	$r_{to} = 1.96 \pm 0.08$ kpc
Position angle (gas) [a]	PA = 127.6 ± 0.3°
Inclination (gas) [a]	$i = 65.5 \pm 0.3°$
Velocity dispersion (gas) [a]	$\sigma_{gas} = 12.4 \pm 1.2$ km s^{-1}
Effective radius (gas) [a]	$R_e = 8.38 \pm 0.05$ kpc
Halo properties	
Halo mass	$\log(M_h/M_\odot) = 12.1 \pm 0.1$
Virial radius	$R_{vir} = 159 \pm 13$ kpc
Dark matter halo velocity dispersion	$\sigma_{DM} \approx 104$ km s^{-1}
Halo maximum circular velocity [g]	$V_{circ} \approx 200$ km s^{-1}
Escape velocity [g]	$V_{esc}(r = 10\,\mathrm{kpc}) \approx 560$ km s^{-1}
Escape velocity [g]	$V_{esc}(r = 50\,\mathrm{kpc}) \approx 460$ km s^{-1}

Notes. [a]In the reconstructed absorber plane. [b]Corrected by magnification adopting $\mu = 1.89$. [c]Obscured. [d]Defined from the arctan rotation curve: $v(r) = v_{max} \arctan(r/r_{to})$. [e]From HST/F814W imaging. [f]Assuming negligible disc thickness. [g]Assuming a NFW profile with concentration parameter $c = 5$.

6. Results

The intervening absorption lines detected along arc B and toward G1 exhibit similar velocities. Given that G1 is an isolated galaxy, we therefore assume that it is responsible for these absorption features (see Sect. 5). Sightlines intersecting the continuum of arc B thus provide transverse probes through the full extent of the CGM, whereas those intersecting the continuum of G1 correspond to down-the-barrel sightlines probing only foreground gas along the line of sight. The transverse sightlines span impact parameters in the range ∼10−50 kpc, corresponding to ∼0.05−0.3 R_{vir}, and are closely aligned with the minor axis of G1 ($\phi \sim 90°$).

6.1. Absorption strength

Figure 5, panel a, shows $W_r(2796)$ as a function of ρ. We compare our transverse $W_r(2796)$ measurements to both quasar–galaxy pairs (Nielsen et al. 2013b; Huang et al. 2021) and other

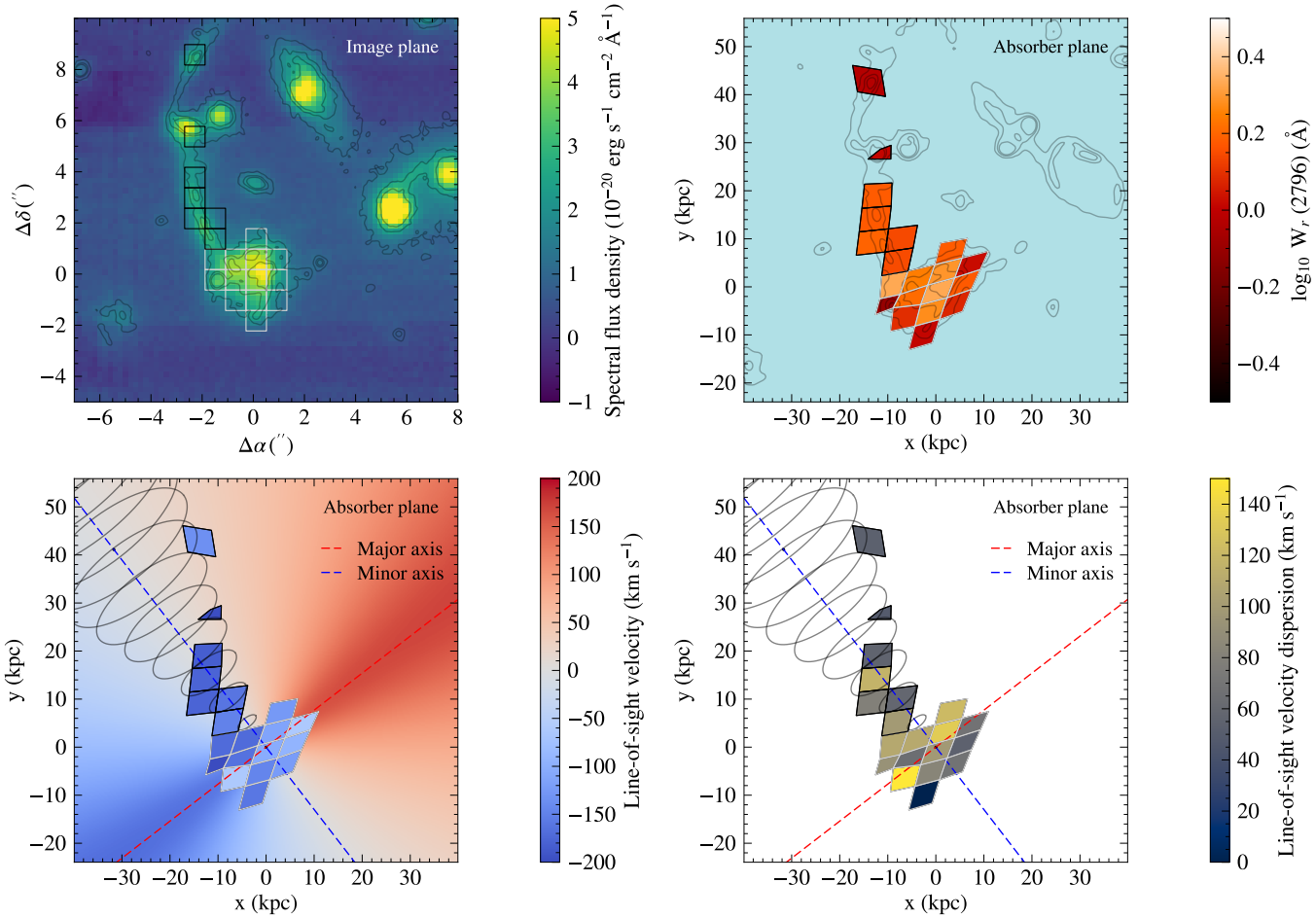

Fig. 4. *Top left*: image-plane (i.e. as observed) MUSE pseudo-broad-band image (SDSS r) around G1 and the background gravitational arc B. The open squares show the 4 × 4-binned spaxels with detected Mg II absorption. Spaxels with black (white) edges correspond to transverse (down-the-barrel) sightlines. *Top right*: absorber-plane (de-lensed) distribution of the measured Mg II equivalent widths $W_r(2796)$. Contours of the de-lensed HST/F814W image of the field are shown for spatial reference. Cluster galaxies and other non-lensed sources should not appear in the absorber plane, but we included them in the contours to provide a spatial reference. *Bottom left*: absorber-plane distribution of the Mg II line-of-sight velocities with respect to z_{G1}. The background colourmap shows the projected line-of-sight velocity of the ERD model for G1. The kinematic major and minor axes of G1 are indicated with the dashed red and blue lines, respectively. The solid black ellipses show a schematic model of a conical outflow along the minor axis of G1, with opening angle $\theta_c = 17.8°$ and inclination $i = 65.5°$. *Bottom right*: absorber-plane distribution of the Mg II line-of-sight velocity dispersion after subtracting the MUSE instrumental LSF in quadrature. The black curves and the dashed red and blue lines indicate the same outflow model and kinematic axes of G1 as in the bottom left panel.

arc tomography systems (Lopez et al. 2018, 2020; Tejos et al. 2021; Shaban et al. 2025). Our measurements fall within the scatter of the quasar statistics (Huang et al. 2021) and the log-linear fit from Nielsen et al. (2013b), and are also encompassed by the scatter of the ensemble of arc tomography systems (Lopez et al. 2018, 2020; Tejos et al. 2021; Shaban et al. 2025). We exclude the down-the-barrel measurement from the $W_r(2796)$–ρ analysis because impact parameters are not defined for this geometry and these sightlines cross half of the CGM from the inside out.

A Pearson correlation analysis for $W_r(2796)$ versus ρ yields a Pearson correlation coefficient $r_P = -0.75$ and p-value $p = 0.026$, confirming a statistically significant anti-correlation, a trend that aligns with previous quasar and arc-based measurements (e.g. Nielsen et al. 2013a; Huang et al. 2021; Lopez et al. 2018). In terms of normalization, our transverse $W_r(2796)$ measurements along the minor axis, lie near the upper envelope of the $W_r(2796)$–ρ space of the combined arc tomography systems over the ∼10−50 kpc range.

6.2. Absorption kinematics

Both down-the-barrel and transverse absorptions along the minor axis of G1 exhibit comparable velocities, with down-the-barrel line-of-sight velocities spanning $v_{los,dtb} = [-63, -239]\,km\,s^{-1}$ and transverse velocities spanning $v_{los,\perp} = [-134, -197]\,km\,s^{-1}$ (Fig. 4 and Table E.1). The blueshifted down-the-barrel absorptions alone already indicate the presence of outflowing gas (e.g. Rubin et al. 2014), and the coherent blueshifts along the minor-axis sightlines of G1 indicate this outflow extends to tens of kiloparsecs (i.e. CGM scales; alternative scenarios are discussed in Sect. 7.1.2). The velocity range probed by $v_{los,dtb}$ is comparable to that spanned by $v_{los,\perp}$, although $v_{los,dtb}$ extends to slightly lower velocities. This likely reflects contributions from absorbing components at or near the systemic velocity of G1, which are unresolved in our data.

Interpreting the CGM kinematics requires placing the absorption velocities in the context of the host galaxy dynamics.

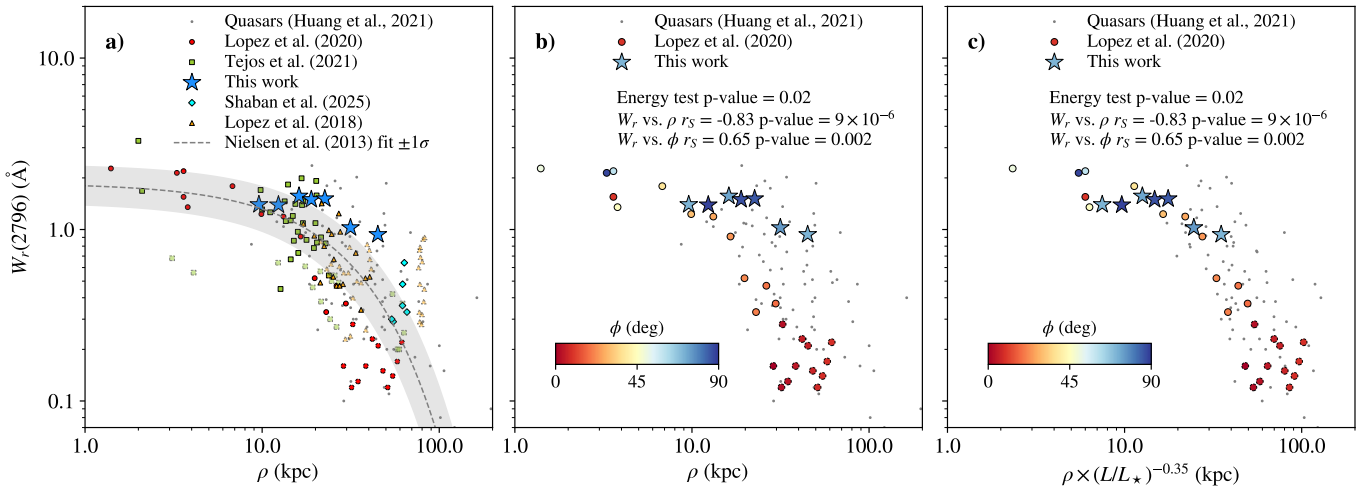

Fig. 5. *Panel a*: rest-frame Mg II equivalent width, $W_r(2796)$, as a function of impact parameter, ρ, relative to the absorber galaxy. Our arc tomography measurements are shown as blue stars. The black dots represent quasar–galaxy pairs at $z \lesssim 0.5$ from Huang et al. (2021). The dashed grey line and shaded region correspond to the log-linear fit ($\pm1\sigma$) from Nielsen et al. (2013b) based on the MAGIICAT sample at $0.07 \leq z \leq 1.1$. The coloured and semi-transparent symbols show individual measurements and upper limits, respectively, from gravitational arc systems from Lopez et al. (2018), Lopez et al. (2020), Tejos et al. (2021), and Shaban et al. (2025). *Panel b*: comparison between the system presented in this work (probed primarily along the minor axis) and that from Lopez et al. (2020, probed along the major axis). The symbols are colour-coded by azimuthal angle ϕ of each sightline relative to the major axis of the absorber galaxy. Overlaid are the results of statistical analyses, including the Energy test statistic and partial Pearson correlation coefficients between $W_r(2796)$ and ρ, and $W_r(2796)$ and ϕ. *Panel c*: same as Panel b, but with impact parameters scaled by the B-band absolute magnitude of the absorbing galaxy using Eq. (2), following Chen et al. (2010)

Previous studies have shown that strong Mg II absorbers may either co-rotate with the stellar disc of the host galaxy (e.g. Ho et al. 2017; Zabl et al. 2019) or trace collimated outflows at kiloparsec scales (e.g. Kacprzak et al. 2014; Zabl et al. 2020). In most quasar–galaxy pair studies, however, these scenarios remain difficult to distinguish because each galaxy is usually probed by a single transverse sightline. Gravitational-arc tomography overcomes this limitation by providing multiple contiguous sightlines through the CGM. By comparing the absorption kinematics with those of the absorbing galaxy, previous arc tomography studies have revealed cases of CGM gas co-rotating with the stellar disc (Lopez et al. 2020; Tejos et al. 2021; Fernandez-Figueroa et al. 2022).

To test the co-rotation scenario, we constructed an extended rotating disc (ERD) model, following Tejos et al. (2021), based on the kinematic model of G1. Starting from the parameters of the arctan model (PA, r_t, $v_{\rm max}$, i), we extrapolated the projected velocity field beyond the stellar disc. The resulting ERD line-of-sight velocity field is shown along with the [O II] centroid-velocity map in Fig. 3, and with the absorption kinematics in Fig. 4, panel c. The absorption velocities clearly differ from those predicted by the ERD model, indicating that the gas kinematics are not explained by disc co-rotation. Although the ERD model does not account for beam-smearing effects introduced by the PSF, this limitation does not affect the qualitative conclusion, as the velocity offsets between the data and the model are large and systematic.

Finally, the absorption kinematics exhibit a remarkable degree of coherence. $v_{\rm los}$ and $\sigma_{\rm los}$ show little scatter across the transverse sightlines, with the scatter in $v_{\rm los}$ of $\sigma_{\rm v,los} \approx 20\,{\rm km\,s^{-1}}$, and the scatter in $\sigma_{\rm los}$ of $\sigma_{\sigma,\rm los} \approx 24\,{\rm km\,s^{-1}}$. Notably, the $\sigma_{\rm v,los}$ value is approximately four times smaller than the mean velocity dispersion $\bar{\sigma}_{\rm los} \approx 72\,{\rm km\,s^{-1}}$. Together, these properties point to a coherent, large-scale, blueshifted structure extending across tens of kiloparsecs, consistent with the presence of a galactic-scale outflow pointing towards the observer.

6.3. Outflow interpretation

6.3.1. Outflow geometry

The predominantly blueshifted Mg II absorptions relative to the systemic velocity of G1 argue strongly against an isotropic outflow. In such a scenario, we would expect symmetric absorption profiles in the transverse direction, combining contributions from both the approaching and receding sides of the outflow bubble, and velocity centroids close to the systemic redshift. However, none of the transverse sightlines show significant absorption at redshifted velocities (Fig. F.1). This, together with the blueshifted down-the-barrel absorptions, indicates that the absorbing material lies entirely on the near side of the galaxy and that the outflow is collimated rather than spherical.

To understand the spatial configuration of the outflowing gas, we modelled the outflow as a bi-conical structure originating from the galaxy centre (e.g. Gauthier & Chen 2012). We used the azimuthal angles of the transverse sightlines (Table E.1) to constrain the outflow opening angle. To intercept all transverse absorptions, the cone must have a minimum half-opening angle of $\theta_{\rm c,min} = 17.8°$. Assuming uniform gas density within the cone (following Chen et al. 2014) and accounting for the galaxy inclination, the geometry must satisfy $i + \theta_{\rm c} \lesssim 90°$ to avoid redshifted transverse absorption features, which restricts the maximum opening angle to $\theta_{\rm c,max} \sim 24.5°$. A schematic of the inferred geometry is shown in Fig. 4.

This narrow opening angle ($\sim$18°–25°) lies below typical values of $\sim$50° inferred from outflow detection rates in inclined galaxies (Martin et al. 2012; Rubin et al. 2014), but aligns with individual quasar-based constraints of $\sim$6°–56° (Gauthier & Chen 2012; Schroetter et al. 2019) and arc tomography estimates ($\theta \sim 36°$; Fernandez-Figueroa et al. 2022). Extended background sources sampling a wider range of azimuthal angles (e.g. Tejos et al. 2021; Fernandez-Figueroa et al. 2022) will be essential to better constrain outflow geometries.

6.3.2. Outflow velocity profile

The unique alignment of the background arc with the minor axis of G1 allows us to trace outflow velocities all the way from the disc of G1 to CGM scales. Assuming a collimated wind (Rubin et al. 2014; Martin 2005; Weiner 2009; Martin et al. 2012) outflowing perpendicular to the disc of G1, we de-projected the transverse impact parameters into a radial distance to the centre of G1 as $r = \rho/\sin i \approx 1.1 \times \rho$. Line-of-sight velocities were likewise de-projected as $v_{\rm depr} = v_{\rm los}/\cos i \approx 2.4 \times v_{\rm los}$.

With these assumptions, we obtained de-projected velocities of $v_{\rm depr,dtb} = 150{-}576\,{\rm km\,s^{-1}}$ for the down-the-barrel sightlines, and $v_{\rm depr,\perp} = 318{-}477\,{\rm km\,s^{-1}}$ for the transverse ones. In Fig. 6, we show $v_{\rm los,\perp}$, $v_{\rm los,dtb}$, $\sigma_{\rm los}$, $v_{\rm depr,\perp}$, and $v_{\rm depr,dtb}$ as a function of r. For the down-the-barrel sightlines, we arbitrarily defined $r = 0$ because the physical scales probed by these sightlines are unknown, while explicitly not assuming that the absorption originates at this distance.

Using the dark matter halo model described in Sect. 4.2 and Appendix B, we computed the expected escape-velocity profile $V_{\rm esc}(r)$, also shown in Fig. 6. The $v_{\rm depr,\perp}$ values approach but do not exceed $V_{\rm esc}(r)$, suggesting that the outflowing material is gravitationally bound to G1. Similarly, the $v_{\rm depr,dtb}$ lie below $V_{\rm esc}(r)$ for $r < 0.3\,R_{\rm vir}$, with the exception of a single sightline that may exceed the escape velocity depending on the (unknown) radius at which the absorption is produced.

The $v_{\rm depr,\perp}$ (and $v_{\rm los,\perp}$) values increase with radius up to $\sim$0.2 $R_{\rm vir}$ before declining near 0.3 $R_{\rm vir}$, suggesting an initially accelerating and then decelerating wind structure. The apparent decline in velocity observed in Fig. 6, although supported by a single data point, is consistent with previous observations. For example, Kacprzak et al. (2014) report blueshifted down-the-barrel velocities of $45{-}255\,{\rm km\,s^{-1}}$ in a $z \sim 0.2$ galaxy with comparable stellar mass and SFR, but significantly lower transverse velocities ($40{-}80\,{\rm km\,s^{-1}}$) at $\rho \sim 58$ kpc, suggesting outflow deceleration at large radii.

To interpret the velocity profile, we adopted a simple momentum-driven wind model (Murray et al. 2005), which has been shown to provide a reasonable description of the kinematics of cool outflows traced by low-ionization absorption lines (e.g. Heckman et al. 2015). Following Heckman et al. (2015), the inwards force $F_{\rm in} = -M_{\rm c}\nabla\phi(r)$ is determined by the gravitational potential $\phi(r)$ and the cloud mass $M_{\rm c}$, while the outwards force $F_{\rm out} = A_{\rm c}\dot{p}_\star/(4\pi r^2)$ is determined by the momentum injection rate from star formation $\dot{p}_\star = 4.8{\times}10^{33}{\times}\left({\rm SFR}/(M_\odot\,{\rm yr^{-1}})\right)$ dyne. Here, $M_{\rm c} = A_{\rm c}N_{\rm H}\,\mu\,m_{\rm p}$, with $A_{\rm c}$ the cloud cross-section, $N_{\rm H}$ its hydrogen column density, and μ the mean particle mass in units of the proton mass $m_{\rm p}$ (we adopt $\mu \simeq 1.6$, Veilleux et al. 2020). The net force is thus given by $F = F_{\rm out} - F_{\rm in} = M_{\rm c}v(r)\,[dv(r)/dr]$. Solving for the radial velocity profile

$$v(r) = \sqrt{v_0^2 + 2\left[\phi(r_0) - \phi(r)\right] + 2\frac{\dot{p}_\star}{4\pi\mu m_{\rm p} N_{\rm H}}\left[\frac{1}{r_0} - \frac{1}{r}\right]} \qquad (1)$$

where the only free parameters are a normalization v_0 defined at r_0, and $N_{\rm H}$ for a given gravitational potential model. We assumed the same dark matter halo model used for estimating $V_{\rm esc}(r)$. The parameters r_0 and v_0 should not be interpreted as the physical launch radius or initial velocity of the outflow, but rather as normalization parameters of the adopted equation of motion.

A least-squares fit to $v_{\rm depr,\perp}$ versus r results in $r_0 = 5.25$ kpc, $v_0 = 116\,{\rm km\,s^{-1}}$, and $\log(N_{\rm H}/{\rm cm^{-2}}) = 19.96$. The best-fit momentum-driven model trajectory is shown in Fig. 6, and is consistent within 1.5σ with all the transverse data points, capturing the initial acceleration, the subsequent decline in velocity, and the sub-escape velocities. We discuss the implications of the outflow radial velocity profile in Sect. 7.1.1.

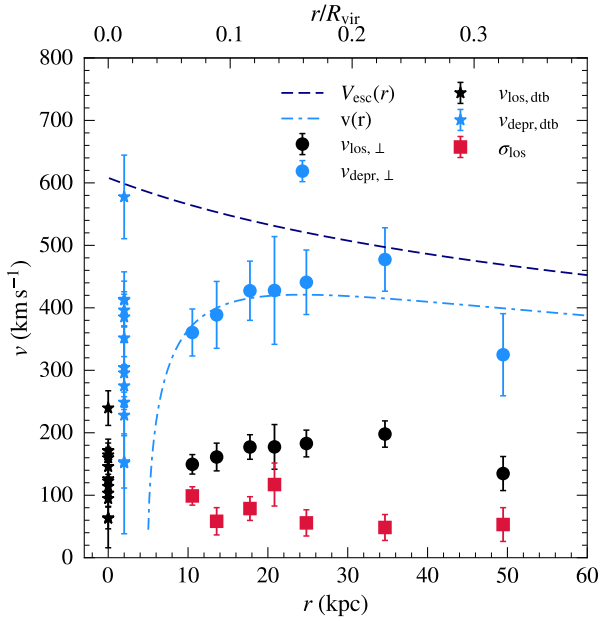

Fig. 6. Velocity profile of the Mg II-traced outflow in G1 as a function of de-projected radius. The black circles show the absolute line-of-sight velocity centroids, $|v_{\rm los,\perp}|$, measured along transverse sightlines probing the projected minor axis of G1, plotted as a function of de-projected galactocentric radius $r = \rho/\sin i$. The light blue circles show the corresponding de-projected velocities, $v_{\rm depr,\perp} = |v_{\rm los,\perp}|/\cos i$, assuming a collimated outflow perpendicular to the disc with inclination $i = 65.5°$. The red squares indicate the line-of-sight velocity dispersions along the transverse sightlines, $\sigma_{\rm los,\perp}$. The black stars at $r = 0$ show the absolute line-of-sight down-the-barrel velocities, $|v_{\rm los,dtb}|$, placed at $r = 0$ for visualisation purposes only, owing to the unknown physical scales probed by these sightlines; the light blue stars offset slightly in r indicate the corresponding de-projected down-the-barrel velocities, $v_{\rm depr,dtb} = |v_{\rm los,dtb}|/\cos i$. The dashed navy curve shows the escape-velocity profile $V_{\rm esc}(r)$ (Sect. 4.2). The dash-dotted light blue curve shows the best-fit momentum-driven wind model $v(r)$ fitted to $v_{\rm depr,\perp}$ vs. r, with best-fit parameters $r_0 = 5.25$ kpc, $v_0 = 116\,{\rm km\,s^{-1}}$, and $\log(N_{\rm H}/{\rm cm^{-2}}) = 19.96$. The top axis indicates the corresponding radial distance in units of the virial radius, $r/R_{\rm vir}$.

6.3.3. Mass outflow rate

With the geometry and kinematics of the outflow characterized, we estimated the associated mass outflow rate. Assuming a thin-shell bi-conical geometry, the instantaneous mass outflow rate at radius r is $\dot{\rm M}_{\rm out} = \Omega\mu m_{\rm p} N_{\rm H} v r$, where $\Omega = \Omega_{\rm outflow}C_{\rm f}$ is the effective solid angle subtended by the outflow, modified by the cloud covering fraction $C_{\rm f}$. As seen from the galaxy, $\Omega_{\rm outflow} = 4\pi\,(1 - \cos\theta)$ for a bi-conical structure. Here, $\mu \simeq 1.6$ is the mean mass per hydrogen atom (accounting for the helium fraction; Veilleux et al. 2020), $m_{\rm p}$ is the proton mass, $N_{\rm H}$ is the total hydrogen column density, and v is the outflow velocity at radius r (Rupke et al. 2005; Veilleux et al. 2020).

We adopted a conservative lower limit on $N_{\rm H\,I}$ derived in Sect. C using Eqs. (C.1) and (C.2), and assume $N_{\rm H} = N_{\rm H\,I}$. With our constraint on the minimum opening angle, we obtained $\Omega_{\rm outflow,min} \approx 0.6$ sr. Also, we assumed $C_{\rm f} \simeq 0.7$ (Berg et al.

2025) measured for Mg II absorption lines against gravitational arcs. Considering the r and $v_{\rm depr,\perp}$ values from Sect. 6.3.1, we estimate a minimum mass outflow rate $\dot{M}_{\rm out,min}\,(r)$, which ranges from $\approx$0.06 $M_\odot\,{\rm yr}^{-1}$ at $\rho \approx 10$ kpc, to $\approx$0.21 $M_\odot\,{\rm yr}^{-1}$ at $\rho \approx 45$ kpc.

From our lower limits on $\dot{M}_{\rm out,min}$ we estimate minimum mass loading factors of $\eta_{\rm min} = \dot{M}_{\rm out,min}/{\rm SFR} \approx (0.4{-}1.5)\times10^{-2}$. Similarly, for the maximum opening angle, the minimum mass outflow rate increases to $\dot{M}_{\rm out,min} \approx (0.12{-}0.4)\ M_\odot\,{\rm yr}^{-1}$ and $\eta_{\rm min} \approx (0.8{-}2.7)\times10^{-2}$. These lower limits are broadly consistent with quasar-traced galactic outflows from MEGAFLOW (Schroetter et al. 2019) and similar studies (e.g. Bouché et al. 2012; Heckman et al. 2015; Martin et al. 2019). Such works typically report $\dot{M}_{\rm out} \sim 0.1{-}10\ M_\odot\,{\rm yr}^{-1}$ and $\eta \sim 0.1{-}10$, albeit with significant scatter and methodological differences.

Our inferred mass loading factors, $\eta_{\rm min} \approx (0.4{-}2.7)\times10^{-2}$, are significantly lower than the predictions from high-resolution zoom-in simulations such as FIRE-2 (Pandya et al. 2021), which suggest $\eta \sim 0.3$ (and typically not exceeding 1) for galaxies with stellar masses $\log(M_\star/M_\odot) \sim 10.3$ at $z \sim 1$. Large-volume simulations such as TNG-50 (Nelson et al. 2019) and EAGLE (Mitchell et al. 2020) predict even higher mass loading factors, $\eta \sim 10$, along with outflow velocities of $\sim$400 km s^{-1} and biconical geometries with opening angles of 40°−50° at similar galactocentric distances. Our measurements therefore provide conservative lower limits that are compatible with these models, but do not allow us to discriminate among them given the uncertainties in geometry, ionization corrections, and column density.

Finally, recent high-resolution simulations of galactic winds (Kim et al. 2020a,b; Schneider et al. 2020; Li & Bryan 2020) explicitly modelling the multiphase nature of outflows indicate that most of the outflowing mass resides in cold and warm ($T \sim 10^4{-}10^5$ K), while most of the energy is carried by hot ($T \sim 10^6{-}10^7$ K) gas. Our Mg II-based measurements trace only the cool component, potentially missing a substantial (and in some models dominant) contribution from the warm and hot phases. A complete census of the mass and energy budget would require constraints on these higher-temperature components, which remain inaccessible with the current data.

7. Discussion

7.1. The smoking gun of a galactic-scale outflow

The collective kinematic signatures observed in both down-the-barrel and transverse sightlines provide compelling evidence for a large-scale, collimated outflow originating from G1. The presence of spatially coherent blueshifted absorption along both the transverse minor-axis and down-the-barrel sightlines is difficult to reconcile with alternative mechanisms (see Sect. 7.1.2). The ratio $v_{\rm los}/\sigma_{\rm los} \sim 2.5$ confirms that bulk motions dominate, and the low scatter in both velocity centroids and dispersions across tens of kiloparsecs suggests a high degree of coherence in the gas dynamics.

Our de-projected velocities inferred along the arc fall within the expected range for outflow velocities (Weiner 2009; Weiner et al. 2009; Martin et al. 2012; Rubin et al. 2014), and are consistent with momentum-driven wind models, which predict outflow velocities of $2{-}3\times V_{\rm circ}$, and close to $V_{\rm esc}$ (e.g. Barai et al. 2013; Katsianis et al. 2017). Our tomographic data also provide, for the first time, a direct observational characterization of the radial velocity profile of a cool outflow at scales of tens of kiloparsecs. The geometry of the background arc allowed us to map $v_{\rm depr,\perp}(r)$ up to ∼50 kpc, revealing a clear acceleration followed by possible deceleration. A simple momentum-driven cloud model (Sect. 6.3.2) seems to reproduce this behaviour: early acceleration arises from the momentum injected by the ongoing star formation, while the deceleration reflects the increasing relative influence of the galaxy's gravitational potential. The model requires column densities of $\log(N_{\rm H\,I}/{\rm cm}^{-2}) \approx 20$ to reproduce the measured velocities, implying that only relatively dense cool clouds can reach several tens of kiloparsecs through this mechanism. However, this column density is as seen from the galaxy radially outwards, and does not necessarily need to match the line-of-sight $N_{\rm H\,I}$.

The values of $\sigma_{\rm los} \approx 50{-}120$ km s^{-1} are comparable to those seen in Mg II absorbers towards background quasars (e.g. Lan & Mo 2018), and similar to values reported in other arc-based studies (Lopez et al. 2020; Tejos et al. 2021; Mortensen et al. 2021). We remark that the observed velocity dispersions are not expected to trace the thermal broadening of the gas. Instead, they likely reflect the kinematics of ensembles of cool, coherent complexes at the kiloparsec scales (e.g. Afruni et al. 2023; Lopez et al. 2024) that are unresolved at the spectral resolution of our observations. High-resolution observations of background quasars generally reveal the presence of multiple narrow components (e.g. Churchill & Vogt 2001) interpreted as discrete clumps, which are expected to be smaller than the spatial sampling of our observations, ∼6 kpc × 6 kpc (see e.g. Chen et al. 2014; Afruni et al. 2023). In this case, the integrated line profiles likely represent the collective motion of such clouds within each spaxel.

These $\sigma_{\rm los}$ values can be interpreted in the context of a biconical outflow geometry with opening angle $\theta_{\rm c}$, which naturally produces a variation in $v_{\rm los}$ in the range $\cos(i-\theta_{\rm c}) \lesssim v_{\rm los}/V \lesssim \cos(i+\theta_{\rm c})$ along a sightline intercepting the axis of the outflow cone, given a radial velocity V and galaxy inclination i. For an opening angle $\theta_{\rm c} = 17.8°$ (see Sect. 6.3.1), and considering G1's inclination, an outflow velocity of $V = 400$ km s^{-1} results in a spread $\Delta v_{\rm los} \approx 200$ km s^{-1}, which may explain the observed line widths considering $\sigma_{\rm los}$ only characterizes 1σ of the full spread of $v_{\rm los}$ and is expected to remain constant if V and $\theta_{\rm c}$ ∼constant. Measuring an azimuthal dependence of $\sigma_{\rm los}$ within an outflow cone will be essential for confirming this projection effect.

The relatively low scatter in $v_{\rm los}$ and $\sigma_{\rm los}$ across tens of kiloparsecs implies a remarkable degree of kinematic coherence of these clouds, both in bulk velocities and integrated motions along the line of sight, further supporting the outflow interpretation if projection effects dominate $\sigma_{\rm los}$. Taken together, the large-scale kinematic coherence, the minor-axis orientation of the sightlines, and the consistency with momentum-driven wind models strongly support a scenario in which the observed gas traces the bulk kinematics of a collimated, galactic-scale outflow, with projection effects likely dominating the observed velocity dispersions.

7.1.1. Signatures of gas recycling

Our results show that the outflow plays a key role in sustaining cool, metal-enriched gas within the CGM of G1, injecting metals out to at least 0.3 $R_{\rm vir}$. The de-projected velocities remain below the halo escape velocity, indicating that most of the ejected material is gravitationally bound and might eventually recycle back onto the galaxy. Single-sightline-probed galactic winds (Bouché et al. 2012; Schroetter et al. 2019) indicate that cool outflows traced by Mg II absorption hardly reach the escape velocities of halos for galaxies between $10 < \log(M_\star/M_\odot) < 11$. In the broader CGM context, Mg II absorption is typically

concentrated within the inner halo, with the bulk of absorbers residing at $\lesssim 0.3\ R_{\rm vir}$, and with rapidly declining covering fractions beyond $\sim 0.3-0.5\,R_{\rm vir}$ (Nielsen et al. 2013b; Huang et al. 2021). Our detection of cool gas out to $0.3\,R_{\rm vir}$ therefore places G1 at the characteristic outer edge where strong Mg II-bearing clouds remain common in star-forming halos at $z \sim 1$.

The sub-escape velocities and the apparent deceleration at $\sim 0.3\,R_{\rm vir}$ suggest that the bulk of the cool outflowing gas is confined within the inner halo, where it may mix with the ambient CGM or be recycled back onto the galaxy. The suppression of Mg II absorption beyond this radius, as seen in galaxy–quasar pair studies (Churchill et al. 2013a), further supports this interpretation. However, since the deceleration in our system is inferred from a single outer sightline, additional tomographic constraints at larger impact parameters are required to confirm this behaviour in individual systems.

The presence of cool gas at $0.3\,R_{\rm vir}$ implies a travel time of ~ 100 Myr, corresponding to a recycling timescale of at least ~ 200 Myr, which is consistent with cosmological simulations predicting that most of the recycling occurs within $0.3\,R_{\rm vir}$ with median recycling timescales of 100−350 Myr at these redshifts. Assuming a constant $\dot{M}_{\rm out} = 0.2\,M_{\odot}\,{\rm yr}^{-1}$, which is reasonable because the UV and emission-line-based SFRs are consistent (an indicator of steady star formation in the last few hundred megayears, Kennicutt & Evans 2012), we obtain a minimum processed gas mass of $0.4 \times 10^8\,M_{\odot}$ stored within the CGM of G1. We emphasize that this result is based on a lower limit on $\dot{M}_{\rm out}$, and that Mg II traces only the cool phase; therefore, this reservoir mass should be regarded as a lower limit to the total recycled mass in the halo.

7.1.2. Alternative scenarios

To assess whether the absorbing gas could originate from mechanisms other than outflows, we consider several alternatives. First, we disfavour ram-pressure stripping and tidal tails. G1 is isolated, with no neighbouring galaxies within $3000\,{\rm km\,s^{-1}}$ in redshift and $500\,{\rm kpc} \times 500\,{\rm kpc}$ in projected area. Moreover, tidal tails are typically narrow (a few kiloparsecs; see e.g. Bonaca et al. 2020), making it unlikely for our extended arc, spanning tens of kiloparsecs in projection, to align by chance with such a structure.

A pressure-supported CGM is also disfavoured. Although the measured $\sigma_{\rm los}$ values are comparable to the expected dark matter halo velocity dispersion of $\sigma_{\rm DM} \approx 104\,{\rm km\,s^{-1}}$, our data show that velocity offsets clearly dominate over the observed dispersions, with a mean ratio $v_{\rm los}/\sigma_{\rm los} \sim 2.5$. In a pressure-supported medium, one would instead expect dispersion-dominated kinematics with no systematic velocity shifts, whereas our measurements favour ordered bulk motions.

We further disfavour accretion in the form of an extended rotating disc. The transverse absorptions arise along the projected minor axis and exhibit kinematics inconsistent with co-planar rotation (see Sect. 4.3). A contribution from co-rotating ISM embedded within the down-the-barrel absorption cannot be completely excluded; however, isolating such a component would require higher spectral resolution and S/N.

Another interpretation is that the transverse sightlines probe radial inflows on the far side of the galaxy. While we cannot entirely rule out this possibility, down-the-barrel absorptions unambiguously indicate a galactic outflow towards the observer. Considering that $v_{\rm dtb}$ and $v_{\perp}$ have similar values and are both oriented along the minor axis, the simplest and most self-consistent explanation is that the transverse absorptions probe the same outflow.

7.2. Azimuthal versus luminosity dependence on $W_r(2796)$

Several studies have found strong evidence for a bi-modality in the azimuthal distribution of Mg II absorbers using both individual background sources (e.g. Kacprzak et al. 2012; Schroetter et al. 2019; Martin et al. 2019; Lundgren et al. 2021) and stacked spectroscopy (Bordoloi et al. 2011), particularly in inclined blue star-forming galaxies. Stronger Mg II equivalent widths are also preferentially found along the minor axis of galaxies (Martin et al. 2019; Schroetter et al. 2019; Lundgren et al. 2021). The usual interpretation is that this bi-modality arises because of outflows and co-planar accretion in the form of extended discs, which are expected to emerge along the minor and major axes, respectively. Arc tomography results support this picture: Tejos et al. (2021) and Fernandez-Figueroa et al. (2022) identified a mild azimuthal correlation in Mg II, consistent with a composite CGM made of bi-conical outflows and extended discs, while Lopez et al. (2020) found evidence for an extended co-rotating disc along the major axis of their absorber galaxy (G1-0311 hereafter). In our study, the absorbing galaxy (G1-0224, for the following discussion) is probed predominantly along the minor axis, where we find strong evidence for the presence of an outflow. Although our transverse sightlines do not sample the full range of azimuthal angles, the fact that G1-0224 and G1-0311 are probed close to the minor and major axes, respectively, provides a useful comparison to assess how $W_r(2796)$ varies with geometry.

Despite their different orientations, both systems show low intrinsic scatter in their individual W_r–ρ relations, indicating coherent cool gas structures over scales of tens of kiloparsecs. When considered together, however, they span much of the scatter seen in quasar-based Mg II samples (Fig. 5b). Importantly, the two galaxies differ substantially in $M_{\star}$, M_B, and SFR: G1-0224 is ≈ 4 times more massive and ≈ 20 times more luminous in the B band than G1-0311, which is transitioning towards quiescence.

The Mg II absorption strongly correlates with host galaxy properties such as stellar mass and luminosity (e.g. Chen & Tinker 2008; Chen et al. 2010; Bordoloi et al. 2011). Chen et al. (2010) showed that much of the W_r–ρ scatter can be reduced by scaling the impact parameters with B-band luminosity:

$$\log \rho_{L_{\star}} = \log \rho \times (L_B/L_{B_{\star}})^{-0.35}. \quad (2)$$

This implies that the extent of the cool, Mg II-bearing CGM grows with galaxy luminosity. This is one manifestation of the self-similar CGM proposed by Churchill et al. (2013b), in which galaxies of different luminosities and masses follow a common W_r–$(\rho/R_{\rm vir})$ relation.

To disentangle the effects of azimuthal angle and luminosity on $W_r(2796)$, we calculated partial Spearman rank correlations while accounting for the natural degeneracy between ϕ and ρ introduced by the arc geometries. Considering both G1-0224 and G1-0311, we find a strong anti-correlation between $W_r(2796)$ and ρ (Spearman rank correlation coefficient r_S and associated p-value; $r_S = -0.83$, $p = 9 \times 10^{-6}$), as expected from quasar-based studies (Nielsen et al. 2013b; Huang et al. 2021), but only a moderate but statistically significant correlation with ϕ ($r_S = 0.65$, $p = 0.002$). Scaling ρ using Eq. (2) weakens the $W_r(2796)$-ϕ correlation ($r_S = 0.31$, $p = 0.18$), whereas the W_r–$\rho_{L_{\star}}$ remains highly significant ($r_S = -0.87$, $p = 10^{-6}$).

A multivariate energy test shows that the original W_r–ρ distributions of the two galaxies differ ($p = 0.03$), but become statistically consistent after luminosity scaling ($p = 0.22$). This confirms that B-band luminosity reduces the scatter in the W_r–ρ relation, implying that part of the large dispersion in quasar absorber statistics reflects the heterogeneity of the galaxy population, and also that the W_r–ρ anti-correlation has a similar shape along both the major and minor axes once host properties are accounted for.

This result must be interpreted with care. The apparent similarity of the W_r–ρ profiles for G1-0224 and G1-0311 does not contradict the well-established azimuthal trends derived from large Mg II absorber samples, which demonstrate a statistical excess of absorbers along galaxy minor axes. Instead, our analysis shows that in two well-characterized halos, one probed near the minor axis (G1-0224) and the other near the major axis (G1-0311), the W_r–ρ relations are essentially indistinguishable once scaled by host luminosity (and thus indirectly by halo mass or size). Despite sampling geometries traditionally associated with different physical processes (outflows along the minor axis, extended discs or inflows along the major axis), the cool gas absorption strength declines with radius in nearly the same way in these two systems. This does not refute the existence of azimuthal bi-modality; rather, it shows that projected geometry alone does not guarantee a significant difference in W_r at fixed ρ. Host galaxy properties, such as luminosity, stellar mass, SFR, may exert a stronger influence on the absorber strength than the projected orientation of the sightlines. Determining whether this is a general feature of individual systems or specific to the particular evolutionary states of G1-0224 and G1-0311 will require a larger sample of arc tomography systems.

8. Summary and conclusions

We have conducted a spatially resolved study of the cool CGM surrounding G1, a luminous (2.6 L_B^*), star-forming (SFR $\approx 15\,M_\odot\,yr^{-1}$), and relatively massive ($\log(M_\star/M_\odot) \approx 10.3$) main-sequence galaxy at $z \sim 1$. The fortuitous alignment of a background gravitational arc enabled us to probe metal absorption lines arising from the CGM of G1 in both down-the-barrel and transverse sightlines, spanning projected distances from the galactic centre out to ~50 kpc along the minor axis. This unique configuration revealed a galactic-scale outflow emerging along the minor axis of G1, allowing us to characterize its geometry and kinematics with unprecedented spatial resolution for absorption-line studies. Our main findings are summarized as follows:

(I) Spatially coherent, blueshifted metal absorption lines detected along the minor axis of a star-forming galaxy, extending out to projected distances of ~50 kpc, provide strong evidence for the detection of a large-scale outflow traced in absorption using gravitational-arc tomography.

(II) The data disfavour a spherical or isotropic outflow geometry, and instead support a collimated wind emerging along the minor axis with opening angle ~18°–25°, minimum mass outflow rate $\dot{M}_{\rm min,out} \sim 0.06$–$0.4\ M_\odot\,yr^{-1}$, and mass loading factor of $\eta_{\rm min} \sim 0.004$–$0.027$, measured within a projected distance of 10–50 kpc. These values are broadly consistent with expectations from cosmological simulations.

(III) The transverse and down-the-barrel absorptions show strong blueshifts, with values up to ~240 km s^{-1}. Combined with relatively low $\sigma_{\rm los}$ values, this implies that the gas is dominated by bulk motion ($v_{\rm los}/\sigma_{\rm los} \sim 2.5$). The small scatter in $v_{\rm los}$ and $\sigma_{\rm los}$ points to high kinematic coherence over tens of kiloparsecs.

(IV) A momentum-driven wind model appears to describe the radial profile of the outflowing cool gas. An initial acceleration of $v_{\rm depr,\perp}$ can be explained by momentum injection from the star formation, and a subsequent deceleration dominated by the gravitational potential. Both the measured $v_{\rm depr,\perp}$ values and the momentum-driven cloud model indicate that the gas barely reaches the escape velocity of the halo, and is likely to be retained within the halo. We estimate a recycling timescale of ~200 Myr, implying a minimum processed gas mass of $0.4\times10^8\ M_\odot$, in the CGM of G1, within 0.3 $R_{\rm vir}$.

(V) Our measurements of $W_r(2796)$ are statistically consistent with the canonical W_r–ρ anti-correlation established from quasar–galaxy pairs. Notably, the scatter in our measurements is small and comparable to that in previous arc tomography studies, supporting the scenario that a significant fraction of the scatter in the quasar statistics is driven by heterogeneity in the host-galaxy properties.

(VI) Compared with a previously studied arc system probing the major axis (Lopez et al. 2020), our minor-axis sightlines yield systematically higher $W_r(2796)$ values. However, once the impact parameters are scaled by the B-band luminosity of the host galaxy, this difference diminishes, and the W_r–ρ distributions become statistically consistent, indicating that major-minor axis alignment does not necessarily guarantee smaller or larger $W_r(2796)$ after accounting for host-galaxy properties.

Our findings provide direct evidence of the physical connection between galactic outflows and the cool metal-bearing CGM. By resolving its structure and kinematics across tens of kiloparsecs, we offer new constraints on the geometry, extent,and kinematics of feedback-driven winds.

Acknowledgements. We thank the anonymous referee for constructive comments and suggestions that significantly improved the clarity and quality of the manuscript. S.L. and N.T. acknowledge support by FONDECYT grant 1231187. J.H. acknowledges support from Beca ANID Doctorado Nacional Folio 21230522, J.H. and L.F.B. acknowledge support from ANID BASAL project FB210003, FONDECYT projects 1230231, and CASSACA project CCJRF1906. Based on observations collected at the European Southern Observatory under ESO programme 094.A-0141 (PI: SWINBANK). This research is partly based on observations made with the NASA/ESA *Hubble* Space Telescope obtained from the Space Telescope Science Institute, which is operated by the Association of Universities for Research in Astronomy, Inc., under NASA contract NAS 5–26555. These observations are associated with programme GO 14497 (PI Smit), and GO 9135 (PI Gladders). This research has made use of the Astrophysics Data System, funded by NASA under Cooperative Agreement 80NSSC21M00561. This work made use of Astropy: a community-developed core Python package and an ecosystem of tools and resources for astronomy. This work also thanks contributors to `GalPak`^{3D}, `MPDAF`, `BAGPIPES`, `NumPy`, `SciPy`, `Matplotlib`, `LINETOOLS`, the `PYTHON` programming language, and the free and open-source community (`www.astropy.org` (Astropy Collaboration 2013, 2018, 2022); `galpak3d.univ-lyon1.fr` (Bouché et al. 2015); `mpdaf.readthedocs.io` (Bacon et al. 2016); `bagpipes.readthedocs.io/` (Carnall et al. 2018, 2019); `numpy.org/` (Harris et al. 2020); `scipy.org` (Virtanen et al. 2020); `matplotlib.org` (Hunter 2007); `linetools.readthedocs.io` (Prochaska et al. 2017); `https://www.python.org/`)

References

Afruni, A., Fraternali, F., & Pezzulli, G. 2021, MNRAS, 501, 5575
Afruni, A., Lopez, S., Anshul, P., et al. 2023, A&A, 680, A112
Anand, G. S., Mack, J., Avila, R. J., et al. 2025, The DrizzlePac Handbook, 3
Astropy Collaboration (Robitaille, T. P., et al.) 2013, A&A, 558, A33
Astropy Collaboration (Price-Whelan, A. M., et al.) 2018, AJ, 156, 123

Astropy Collaboration (Price-Whelan, A. M., et al.) 2022, ApJ, 935, 167
Bacon, R., Accardo, M., Adjali, L., et al. 2010, SPIE Conf. Ser., 7735, 773508
Bacon, R., Piqueras, L., Conseil, S., Richard, J., & Shepherd, M. 2016, Astrophysics Source Code Library [record ascl:1611.003]
Barai, P., Viel, M., Borgani, S., et al. 2013, MNRAS, 430, 3213
Berg, T. A. M., Afruni, A., Ledoux, C., et al. 2025, A&A, 693, A200
Bergeron, J., & Stasińska, G. 1986, A&A, 169, 1
Bertin, E., & Arnouts, S. 1996, A&AS, 117, 393
Bonaca, A., Pearson, S., Price-Whelan, A. M., et al. 2020, ApJ, 889, 70
Bordoloi, R., Lilly, S. J., Knobel, C., et al. 2011, ApJ, 743, 10
Bouché, N., Carfantan, H., Schroetter, I., Michel-Dansac, L., & Contini, T. 2015, ApJ, 150, 15
Bouché, N., Hohensee, W., Vargas, R., et al. 2012, MNRAS, 426, 801
Burchett, J. N., Rubin, K. H. R., Prochaska, J. X., et al. 2021, ApJ, 909, 151
Carnall, A. C., McLure, R. J., Dunlop, J. S., & Davé, R. 2018, MNRAS, 480, 4379
Carnall, A. C., McLure, R. J., Dunlop, J. S., et al. 2019, MNRAS, 490, 417
Charlot, S., & Fall, S. M. 2000, ApJ, 539, 718
Chen, H.-W., & Tinker, J. L. 2008, ApJ, 687, 745
Chen, H.-W., Helsby, J. E., Gauthier, J.-R., et al. 2010, ApJ, 714, 1521
Chen, H.-W., Gauthier, J.-R., Sharon, K., et al. 2014, MNRAS, 438, 1435
Child, H. L., Habib, S., Heitmann, K., et al. 2018, ApJ, 859, 55
Churchill, C. W., & Vogt, S. S. 2001, AJ, 122, 679
Churchill, C. W., Steidel, C. C., & Vogt, S. S. 1996, ApJ, 471, 164
Churchill, C. W., Nielsen, N. M., Kacprzak, G. G., & Trujillo-Gomez, S. 2013a, ApJ, 763, L42
Churchill, C. W., Trujillo-Gomez, S., Nielsen, N. M., & Kacprzak, G. G. 2013b, ApJ, 779, 87
Coil, A. L., Weiner, B. J., Holz, D. E., et al. 2011, ApJ, 743, 46
Draine, B. T. 2011, Physics of the Interstellar and Intergalactic Medium (Princeton: Princeton University Press)
Dutta, R., Fumagalli, M., Fossati, M., et al. 2020, MNRAS, 499, 5022
Elahi, P. J., Power, C., Lagos, C. P., Poulton, R., & Robotham, A. S. G. 2018, MNRAS, 477, 616
Elmegreen, D. M., Elmegreen, B. G., Rubin, D. S., & Schaffer, M. A. 2005, ApJ, 631, 85
ESO Cpl Development Team 2015, Astrophysics Source Code Library [record ascl:1402.010]
Faucher-Giguère, C.-A., & Oh, S. P. 2023, ARA&A, 61, 131
Fernandez-Figueroa, A., Lopez, S., Tejos, N., et al. 2022, MNRAS, 517, 2214
Fitzpatrick, E. L. 1999, PASP, 111, 63
Förster Schreiber, N. M., Genzel, R., Bouché, N., et al. 2009, ApJ, 706, 1364
Gauthier, J.-R., & Chen, H.-W. 2012, MNRAS, 424, 1952
Gladders, M. D., Yee, H. K. C., & Ellingson, E. 2002, AJ, 123, 1
Guérou, A., Krajnović, D., Epinat, B., et al. 2017, A&A, 608, A5
Guo, Y., Ferguson, H. C., Bell, E. F., et al. 2015, ApJ, 800, 39
Harris, C. R., Millman, K. J., van der Walt, S. J., et al. 2020, Nature, 585, 357
Heckman, T. M., Alexandroff, R. M., Borthakur, S., Overzier, R., & Leitherer, C. 2015, ApJ, 809, 147
Ho, S. H., Martin, C. L., Kacprzak, G. G., & Churchill, C. W. 2017, ApJ, 835, 267
Huang, Y.-H., Chen, H.-W., Shectman, S. A., et al. 2021, MNRAS, 502, 4743
Hunter, J. D. 2007, Comput. Sci. Eng., 9, 90
Jenkins, E. B. 2009, ApJ, 700, 1299
Jullo, E., Kneib, J. P., Limousin, M., et al. 2007, New J. Phys., 9, 447
Kacprzak, G. G., Churchill, C. W., & Nielsen, N. M. 2012, ApJ, 760, L7
Kacprzak, G. G., Martin, C. L., Bouché, N., et al. 2014, ApJ, 792, L12
Kalita, B. S., Suzuki, T. L., Kashino, D., et al. 2025, MNRAS, 536, 3090
Katsianis, A., Tescari, E., Blanc, G., & Sargent, M. 2017, MNRAS, 464, 4977
Kennicutt, R. C., Jr 1998, ARA&A, 36, 189
Kennicutt, R. C., & Evans, N. J. 2012, ARA&A, 50, 531
Kim, C.-G., Ostriker, E. C., Fielding, D. B., et al. 2020a, ApJ, 903, L34
Kim, C.-G., Ostriker, E. C., Somerville, R. S., et al. 2020b, ApJ, 900, 61
Lan, T.-W., & Fukugita, M. 2017, ApJ, 850, 156
Lan, T.-W., & Mo, H. 2018, ApJ, 866, 36
Lanzetta, K. M., Wolfe, A. M., Turnshek, D. A., et al. 1991, ApJS, 77, 1
Law, D. R., Steidel, C. C., Erb, D. K., et al. 2007, ApJ, 656, 1
Li, M., & Bryan, G. L. 2020, ApJ, 890, L30
Lopez, S., & Krogager, J.-K. 2025, A&A, 703, A21
Lopez, S., Tejos, N., Ledoux, C., et al. 2018, Nature, 554, 493
Lopez, S., Tejos, N., Barrientos, L. F., et al. 2020, MNRAS, 491, 4442
Lopez, S., Afruni, A., Zamora, D., et al. 2024, A&A, 691, A356
Lundgren, B. F., Creech, S., Brammer, G., et al. 2021, ApJ, 913, 50
Martin, C. L. 2005, ApJ, 621, 227
Martin, C. L., & Bouché, N. 2009, ApJ, 703, 1394
Martin, C. L., Shapley, A. E., Coil, A. L., et al. 2012, ApJ, 760, 127
Martin, C. L., Ho, S. H., Kacprzak, G. G., & Churchill, C. W. 2019, ApJ, 878, 84
Matejek, M. S., & Simcoe, R. A. 2012, ApJ, 761, 112
Ménard, B., & Chelouche, D. 2009, MNRAS, 393, 808
Mitchell, P. D., Schaye, J., Bower, R. G., & Crain, R. A. 2020, MNRAS, 494, 3971
Mortensen, K., Keerthi Vasan, G. C., Jones, T., et al. 2021, ApJ, 914, 92
Moster, B. P., Somerville, R. S., Maulbetsch, C., et al. 2010, ApJ, 710, 903
Murray, N., Quataert, E., & Thompson, T. A. 2005, ApJ, 618, 569
Navarro, J. F., Frenk, C. S., & White, S. D. M. 1996, ApJ, 462, 563
Nelson, D., Pillepich, A., Springel, V., et al. 2019, MNRAS, 490, 3234
Nielsen, N. M., Churchill, C. W., & Kacprzak, G. G. 2013a, ApJ, 776, 115
Nielsen, N. M., Churchill, C. W., Kacprzak, G. G., & Murphy, M. T. 2013b, ApJ, 776, 114
Nielsen, N. M., Fisher, D. B., Kacprzak, G. G., et al. 2024, Nat. Astron., 8, 1602
Pandya, V., Fielding, D. B., Anglés-Alcázar, D., et al. 2021, MNRAS, 508, 2979
Patrício, V., Richard, J., Carton, D., et al. 2018, MNRAS, 477, 18
Peng, C. Y., Ho, L. C., Impey, C. D., & Rix, H.-W. 2002, AJ, 124, 266
Péroux, C., & Howk, J. C. 2020, ARA&A, 58, 363
Pessa, I., Wisotzki, L., Urrutia, T., et al. 2024, A&A, 691, A5
Popesso, P., Concas, A., Cresci, G., et al. 2023, MNRAS, 519, 1526
Prochaska, J. X., Tejos, N., Crighton, N., et al. 2017, linetools/linetools: Third Minor Release
Rubin, K. H. R., Weiner, B. J., Koo, D. C., et al. 2010, ApJ, 719, 1503
Rubin, K. H. R., Prochaska, J. X., Ménard, B., et al. 2011, ApJ, 728, 55
Rubin, K. H. R., Prochaska, J. X., Koo, D. C., et al. 2014, ApJ, 794, 156
Rubin, K. H. R., Diamond-Stanic, A. M., Coil, A. L., Crighton, N. H. M., & Stewart, K. R. 2018, ApJ, 868, 142
Rupke, D. S., Veilleux, S., & Sanders, D. B. 2005, ApJS, 160, 115
Savage, B. D., & Sembach, K. R. 1996, ARA&A, 34, 279
Schlafly, E. F., & Finkbeiner, D. P. 2011, ApJ, 737, 103
Schlegel, D. J., Finkbeiner, D. P., & Davis, M. 1998, ApJ, 500, 525
Schneider, E. E., Ostriker, E. C., Robertson, B. E., & Thompson, T. A. 2020, ApJ, 895, 43
Schroetter, I., Bouché, N., Wendt, M., et al. 2016, ApJ, 833, 39
Schroetter, I., Bouché, N. F., Zabl, J., et al. 2019, MNRAS, 490, 4368
Shaban, A., Bordoloi, R., O'Meara, J. M., et al. 2025, ApJ, 986, 190
Shibuya, T., Ouchi, M., Kubo, M., & Harikane, Y. 2016, ApJ, 821, 72
Smit, R., Swinbank, A. M., Massey, R., et al. 2017, MNRAS, 467, 3306
Soto, K. T., Lilly, S. J., Bacon, R., Richard, J., & Conseil, S. 2016, MNRAS, 458, 3210
Steidel, C. C. 1995, in QSO Absorption Lines, ed. G. Meylan, 139
Swinbank, A. M., Bower, R. G., Smith, G. P., et al. 2007, MNRAS, 376, 479
Tejos, N., López, S., Ledoux, C., et al. 2021, MNRAS, 507, 663
Tremonti, C. A., Moustakas, J., & Diamond-Stanic, A. M. 2007, ApJ, 663, L77
Tumlinson, J., Peeples, M. S., & Werk, J. K. 2017, ARA&A, 55, 389
Veilleux, S., Maiolino, R., Bolatto, A. D., & Aalto, S. 2020, A&ARv, 28, 2
Virtanen, P., Gommers, R., Oliphant, T. E., et al. 2020, Nat. Methods, 17, 261
Weilbacher, P. M., Streicher, O., Urrutia, T., et al. 2012, Proc. SPIE, 8451, 84510B
Weiner, B. J. 2009, AIP Conf. Ser., 1201, 142
Weiner, B. J., Coil, A. L., Prochaska, J. X., et al. 2009, ApJ, 692, 187
Willmer, C. N. A., Faber, S. M., Koo, D. C., et al. 2006, ApJ, 647, 853
Zabl, J., Bouché, N. F., Schroetter, I., et al. 2019, MNRAS, 485, 1961
Zabl, J., Bouché, N. F., Schroetter, I., et al. 2020, MNRAS, 492, 4576

Appendix A: Strong lens modelling

We used the publicly available software LENSTOOL (Jullo et al. 2007) to perform parametric modelling of the cluster mass distribution. The model includes a large-scale smooth component representing the cluster dark matter halo and individual mass components associated with cluster galaxies. The mass distributions of both cluster-scale and galaxy-scale halos were modelled as truncated pseudo-isothermal elliptical mass distributions (PIEMDs). For the cluster-scale halo, we adopted a PIEMD potential centred around the brightest cluster galaxy (BCG) at $z_{\rm cluster} = 0.773$. All model parameters—position, velocity dispersion, ellipticity, and position angle—were allowed to vary with broad priors, except for the cut radius, which was fixed to 1000 kpc, well beyond the strong-lensing regime. For the galaxy-scale halos, we included sixteen spectroscopically confirmed cluster members detected in the MUSE data. These galaxies were selected to be within $\pm 3000\,{\rm km\,s^{-1}}$ of the cluster redshift, and within 30″ of the BCG, where strong-lensing constraints are available.

Photometric and morphological properties of the cluster galaxies were measured using SExtractor (Bertin & Arnouts 1996) in the *HST* imaging. We fixed their centroids, position angles, and ellipticities according to their morphology measured by SExtractor. We scaled their velocity dispersions ($\sigma_{\rm LENSTOOL}$), core ($r_{\rm core}$), and cut radius ($r_{\rm cut}$) adopting the scaling relations detailed in Jullo et al. (2007). A reference luminosity L_* was chosen for a galaxy with apparent magnitude $m_{\rm F160W} = 18$. The reference core radius $r^*_{\rm core}$ was fixed to a negligible but non-zero value.

The best-fit parameters for the cluster-scale halo are a velocity dispersion $\sigma_{\rm LENSTOOL} = 632 \pm 45\,{\rm km\,s^{-1}}$, an ellipticity of 0.65 ± 0.1 with a position angle of $45 \pm 1.5°$, and a core radius of $r_{\rm core} = 6.8 \pm 10$ kpc. For a cluster galaxy with reference magnitude $m_{\rm F160W} = 18$, we obtained a best-fit velocity dispersion $\sigma_{\rm LENSTOOL} = 359 \pm 68\,{\rm km\,s^{-1}}$ and cut radius $r_{\rm cut} = 46.2 \pm 64$ kpc. This model achieves an image-plane RMS of 0.79″, with a $\chi^2 = 13.7$ and 11 free parameters.

Appendix B: SED modelling and halo properties

We first modelled the spectral energy distribution (SED) of G1 using BAGPIPES (Carnall et al. 2018,Carnall et al. 2019), jointly fitting its MUSE and HST photometry. The spectrum of G1 was extracted within a 1.5″aperture in the MUSE data, corrected for both lensing magnification and Galactic extinction (using the same procedure as in Sect. 4.1), and is shown in Fig. D.1.

For the SED model, we assumed a double power-law for the star formation history (SFH), and the Charlot & Fall (2000) extinction law (CF00), with uniform priors of $0 < A_V < 2$ and $-4 < n < 4$ for the dust attenuation. A nebular component was included with ionization parameter $-3 \leq \log U \leq -2$. We adopted uniform priors for the stellar velocity dispersion ($50\,{\rm km\,s^{-1}} < \sigma < 300\,{\rm km\,s^{-1}}$), and metallicity ($0.2 < [Z/H] < 4$). The resulting stellar mass and SFR were inferred from the posterior distributions and are listed in Table 1.

Next, we estimated the halo mass $M_{\rm h}$ using the stellar-mass-halo-mass (SMHM) relation from Moster et al. (2010), assuming $M_{\rm h} = M_{200}$. From this, we derived the virial radius via $R_{\rm vir} = [3M_{\rm h}/(4\pi 200\rho_{\rm c}(z))]^{1/3}$ and the maximum circular velocity as $V_{\rm max} = [10M_{\rm h}GH(z)]^{1/3}$, where G is the gravitational constant and $\rho_{\rm c}(z)$ and $H(z)$ are the critical density and Hubble parameter at redshift z, respectively. The halo velocity dispersion was estimated using the scaling relation from Elahi et al. (2018): $\sigma_{\rm DM} \simeq 430\left(M_{\rm h}/10^{14}\,M_\odot\right)^{1/3}\,{\rm km\,s^{-1}}$.

We estimated the escape velocity $V_{\rm esc}(r) = \sqrt{2|\phi(r)|}$ and circular velocity $V_{\rm circ}(r) = \sqrt{r|d\phi(r)/dr|}$ for G1, assuming a Navarro-Frenk-White (NFW, Navarro et al. 1996) gravitational potential $\phi(r)$ for the dark matter (DM) halo, with a concentration parameter of $c = 5$ (for galaxies with similar M_{200} from N-body simulations; Child et al. 2018). Maximum circular velocity and escape velocities at $r = 10$ kpc and $r = 50$ kpc are indicated in Table 1.

Appendix C: Estimation of $N_{\rm H\,I}$

A column density N of an absorbing species, in the optically thin regime, can be estimated as

$$N > 1.130 \times 10^{12}{\rm cm^{-1}}\,\frac{W_r}{f\lambda^2} \tag{C.1}$$

for a given transition, where f, λ, and W_r are its oscillator strength, rest-frame wavelength, and measured rest equivalent width, respectively (Draine 2011). Although the Mg II absorption is likely saturated and unresolved, we adopt the optically thin limit to estimate a conservative lower bound on the column density. Any degree of saturation or unresolved component structure increases the true N above the linear-regime value, making the optically thin approximation a strict lower limit. For $W_r(2796) \sim 1--1.5$ Å we estimate $\log(N_{Mg\,II}/{\rm cm^{-2}}) > 13.4--13.6$.

Following Rubin et al. (2014), the corresponding N_{Mgii} can be used to estimate $N_{\rm H\,I}$ as

$$N_{\rm H\,I} > \frac{10^{19.3}\ {\rm cm^{-2}}}{\chi(Mg{\rm II})}\,\frac{N_{Mg\,II}}{10^{14.4}\ {\rm cm^{-2}}}\,\frac{10^{-4.42}}{10^{\log {\rm Mg/H}}}\,\frac{10^{-0.5}}{10^{d({\rm Mg})}}. \tag{C.2}$$

Assuming a solar abundance ratio $\log {\rm Mg/H} = -4.42$ (Savage & Sembach 1996), unity ionization fraction $\chi(Mg\ {\rm II}) = 1$, and dust depletion factor $d({\rm Mg}) = -0.5$ (Galactic ISM values range between −0.3 and −1.5 Jenkins 2009), we get lower limits of $\log(N_{\rm H\,I}/{\rm cm^{-2}}) > 18.3–18.5$.

Self-shielding is required to retain significant amounts of Mg II in dense clouds. Photoionization models show that Mg II with $\log(N_{Mg\,II}/{\rm cm^{-2}}) \geq 13.4$ can only survive in gas with $\log(N_{\rm H\,I}/{\rm cm^{-2}}) \gtrsim 18$ (Bergeron & Stasińska 1986). Moreover, empirical $W_r(2796)$-$N_{\rm H\,I}$ relations at $0.4 \lesssim z \lesssim 2.5$ based on quasar sightlines (Ménard & Chelouche 2009; Lan & Fukugita 2017) indicate that $\log(N_{\rm H\,I}/{\rm cm^{-2}})$ correlates with $W_r(2796)$, albeit with large scatter; however, absorbers with $W_r(2796)$ between ∼1and1.5 Å span around three orders of magnitude in $\log(N_{\rm H\,I}/{\rm cm^{-2}})$, between 18.3 and 21.6. The inferred values are consistent with the spread in $N_{\rm H\,I}$ from background quasars, and the minimum $N_{\rm H\,I}$ required for self-shielded clouds. We remark that, given our assumptions for saturation, abundance, ionization fraction, and dust depletion, our $N_{\rm H\,I}$ lower limit estimated using Eq. C.2 is extremely conservative, and a direct measurement would almost certainly yield substantially higher column densities.

Appendix D: G1 spectrum

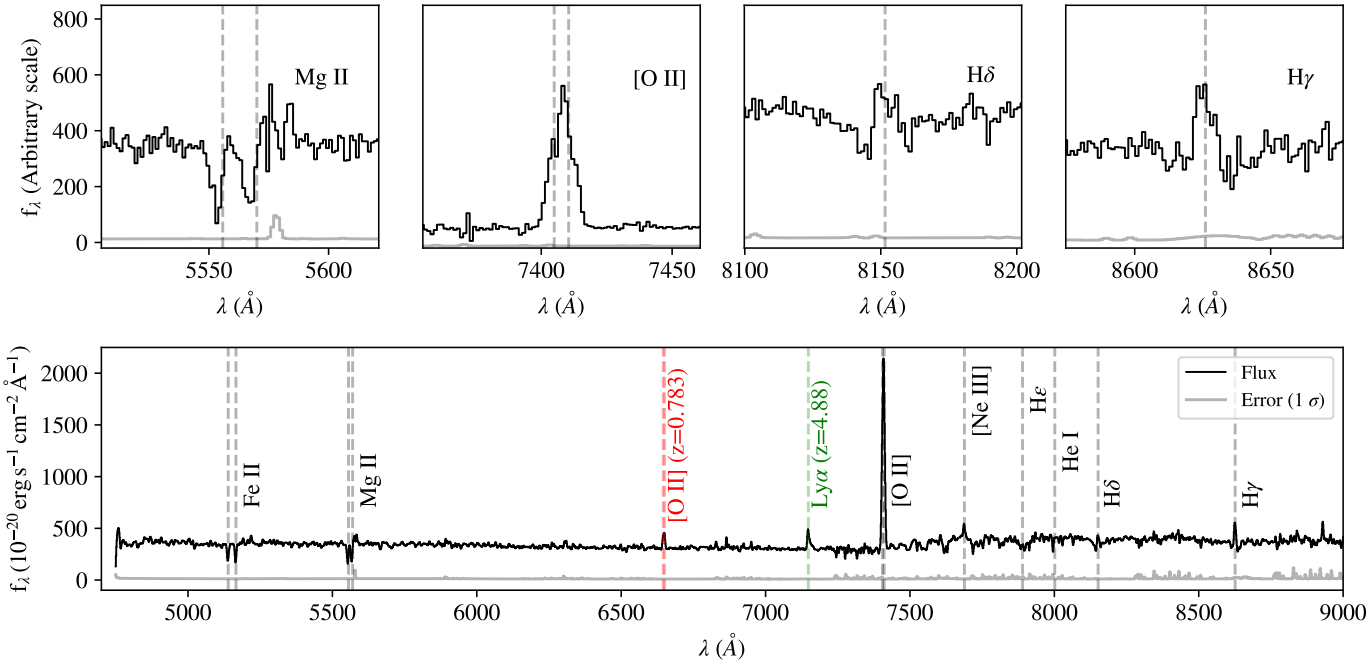

Fig. D.1. *Bottom*: Integrated MUSE spectrum of G1, corrected by Galactic extinction and lensing magnification. The vertical dashed grey lines mark the positions of strong absorption and emission features at z_{G1}. Several narrow emission lines are present, including [O II], Ne III, He I, and Balmer lines. Mg II is blueshifted with respect to the emission lines. Lyα emission is observed at $z \sim 4.88$, corresponding to a counter-image of the arc A, and diffuse [O II] emission from the galaxy cluster at ~0.773 are also present in the spectrum. *Top*: From left to right, zoomed-in images of the Mg II, [O II], Hδ, and Hγ lines.

Appendix E: Spatially resolved absorption-line measurements

Table E.1. Properties of the absorptions measured on the binned MUSE spaxels.

x (pix) (0)	y (pix) (1)	ρ (kpc) (2)	v_{los} (km s^{-1}) (3)	σ_{los} (km s^{-1}) (4)	ϕ (deg) (5)	W_{2586} (Å) (6)	W_{2600} (Å) (7)	W_{2796} (Å) (8)	W_{2803} (Å) (9)	$\mathcal{R}^{\mathrm{Fe\ II}}_{Mg\ II}$ dimensionless (10)
46	31	13.3	...	...	175	< 0.88	< 0.88	< 1.05	< 1.36	...
46	32	10.1	−239 ± 27	92 ± 26	169	1.21 ± 0.38	1.21 ± 0.35	0.78 ± 0.34	< 1.11	1.55 ± 0.81
46	33	9.0	−171 ± 18	108 ± 17	141	1.68 ± 0.37	1.77 ± 0.29	2.13 ± 0.39	1.62 ± 0.55	0.83 ± 0.20
47	31	9.0	−62 ± 47	179 ± 42	−173	1.63 ± 0.55	1.89 ± 0.42	1.23 ± 0.51	< 1.23	1.54 ± 0.72
47	32	6.0	−164 ± 10	64 ± 10	166	1.20 ± 0.24	1.43 ± 0.70	1.62 ± 0.24	< 1.12	0.88 ± 0.45
47	33	4.1	−170 ± 12	109 ± 11	118	1.89 ± 0.27	2.71 ± 1.38	1.75 ± 0.28	< 0.95	1.55 ± 0.82
47	34	6.7	...	...	73	< 0.73	< 0.91	< 1.39	< 1.68	...
48	30	10.2	−159 ± 16	0 ± 63	−141	< 0.93	1.11 ± 0.36	1.03 ± 0.36	0.87 ± 0.37	1.08 ± 0.51
48	31	5.3	−145 ± 12	82 ± 11	−139	1.50 ± 0.30	1.93 ± 0.95	1.88 ± 0.28	1.31 ± 0.38	1.03 ± 0.53
48	32	1.0	−103 ± 10	98 ± 9	−105	1.64 ± 0.23	1.97 ± 0.19	2.14 ± 0.24	1.81 ± 0.42	0.92 ± 0.14
48	33	3.7	−113 ± 14	133 ± 13	21	1.73 ± 0.26	< 0.69	1.96 ± 0.27	1.84 ± 0.70	< 0.18
48	34	8.1	−126 ± 27	121 ± 26	28	1.49 ± 0.44	1.55 ± 0.66	1.51 ± 0.42	< 1.14	1.03 ± 0.53
49	31	5.5	−122 ± 22	68 ± 21	−79	< 0.66	1.43 ± 0.45	1.18 ± 0.38	< 1.28	1.20 ± 0.55
49	32	5.8	−94 ± 12	53 ± 11	−30	1.46 ± 0.30	1.51 ± 0.41	1.49 ± 0.30	1.18 ± 0.31	1.01 ± 0.34
49	33	8.8	−63 ± 17	67 ± 16	−5	1.06 ± 0.30	1.35 ± 0.27	1.05 ± 0.30	1.04 ± 0.44	1.29 ± 0.45
49	34	12.4	...	...	6	< 0.95	< 0.77	< 0.80	< 1.08	...
44	**39**	**32.0**	...	...	**82**	**< 0.80**	**< 0.89**	**< 0.81**	**< 1.46**	...
44	**40**	**33.4**	...	...	**80**	**< 1.05**	**< 0.88**	**< 1.05**	**< 1.09**	...
45	**34**	**14.6**	...	...	**124**	**< 0.89**	**< 0.99**	**< 0.88**	**< 1.56**	...
45	**35**	**16.2**	**−177 ± 19**	**78 ± 18**	**107**	**0.90 ± 0.40**	**1.70 ± 0.70**	**1.57 ± 0.40**	**< 1.46**	**1.08 ± 0.52**
45	**36**	**18.9**	**−177 ± 35**	**117 ± 34**	**93**	**1.23 ± 0.54**	**< 0.76**	**1.50 ± 0.50**	**< 2.25**	**< 0.25**
45	**37**	**22.6**	**−182 ± 21**	**55 ± 20**	**84**	**< 0.91**	**1.00 ± 0.38**	**1.51 ± 0.41**	**0.97 ± 0.40**	**0.67 ± 0.31**
45	**38**	**26.9**	...	...	**78**	**< 0.83**	**< 0.96**	**< 0.78**	**< 0.94**	...
45	**39**	**31.5**	**−197 ± 21**	**48 ± 20**	**75**	**< 0.73**	**< 0.81**	**1.02 ± 0.30**	**0.97 ± 0.26**	**< 0.39**
45	**40**	**30.7**	...	...	**74**	**< 1.45**	**< 1.20**	**< 0.86**	**< 0.93**	...
45	**43**	**45.0**	**−134 ± 27**	**53 ± 27**	**70**	**< 0.79**	**0.74 ± 0.37**	**0.94 ± 0.38**	**< 1.04**	**0.79 ± 0.51**
46	**34**	**9.6**	**−149 ± 15**	**98 ± 14**	**109**	**2.08 ± 0.39**	**< 0.77**	**1.40 ± 0.35**	**1.39 ± 0.26**	**< 0.27**
46	**35**	**12.4**	**−161 ± 22**	**58 ± 21**	**87**	**< 0.78**	**1.19 ± 0.44**	**1.39 ± 0.43**	**< 1.58**	**0.86 ± 0.41**
46	**40**	**30.3**	...	...	**61**	**< 1.10**	**< 1.03**	**< 0.76**	**< 0.82**	...

Notes. (0) x coordinate of the binned spaxel.
(1) y coordinate of the binned spaxel.
(2) Impact parameter; projected physical separation between the centre of the spaxel and the centre of G1, in the absorber plane.
(3) Line-of-sight velocity of the absorption centroid with respect to z_{G1}.
(4) Line-of-sight velocity dispersion after subtracting the instrumental LSF.[a]
(5) Azimuthal angle of the centre of the spaxel with respect to G1 receding major axis.
(6) Fe II 2586Å rest-frame equivalent width.[b]
(7) Fe II 2600Å rest-frame equivalent width.[b]
(8) Mg II 2796Å rest-frame equivalent width.[b]
(9) Mg II 2803Å rest-frame equivalent width.[b]
(10) Ratio between $W_r(2600)$ and $W_r(2796)$.
(a) The value is set to 0 when the observed FWHM is larger than the instrumental FWHM.
(b) Non-detections are reported as 2σ upper limits.

Appendix F: Spatial distribution of Mg II spectra

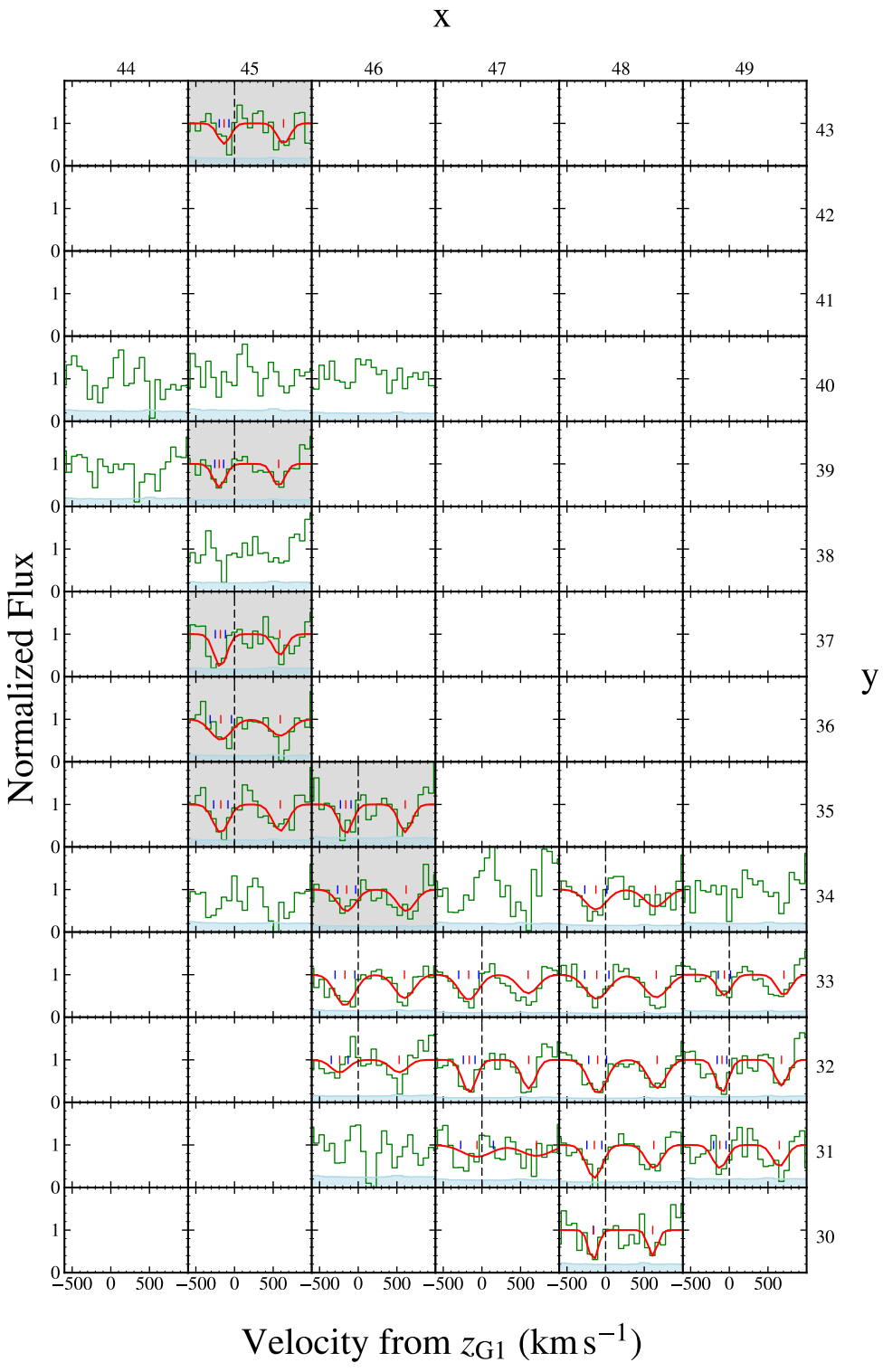

Fig. F.1. Spatial distribution of the Mg II spectra extracted over the arc images B1-B2 meeting the continuum S/N criteria in the image plane. Each panel shows the spectrum in a 4×4 ($0.8'' \times 0.8''$) binned spaxel. The green lines show the observed normalized flux, and the light blue line shows the corresponding 1σ error. The red curves show the fitted Mg II doublet when detected, and the dashed black vertical lines indicate the zero velocity of the Mg II λ2796Å transition at z_{G1}. Spaxels with detected absorption are the same as in Fig. 4. The grey-shaded panels indicate transverse sightlines with detected Mg II absorption.

Appendix G: Spatial distribution of Fe II spectra

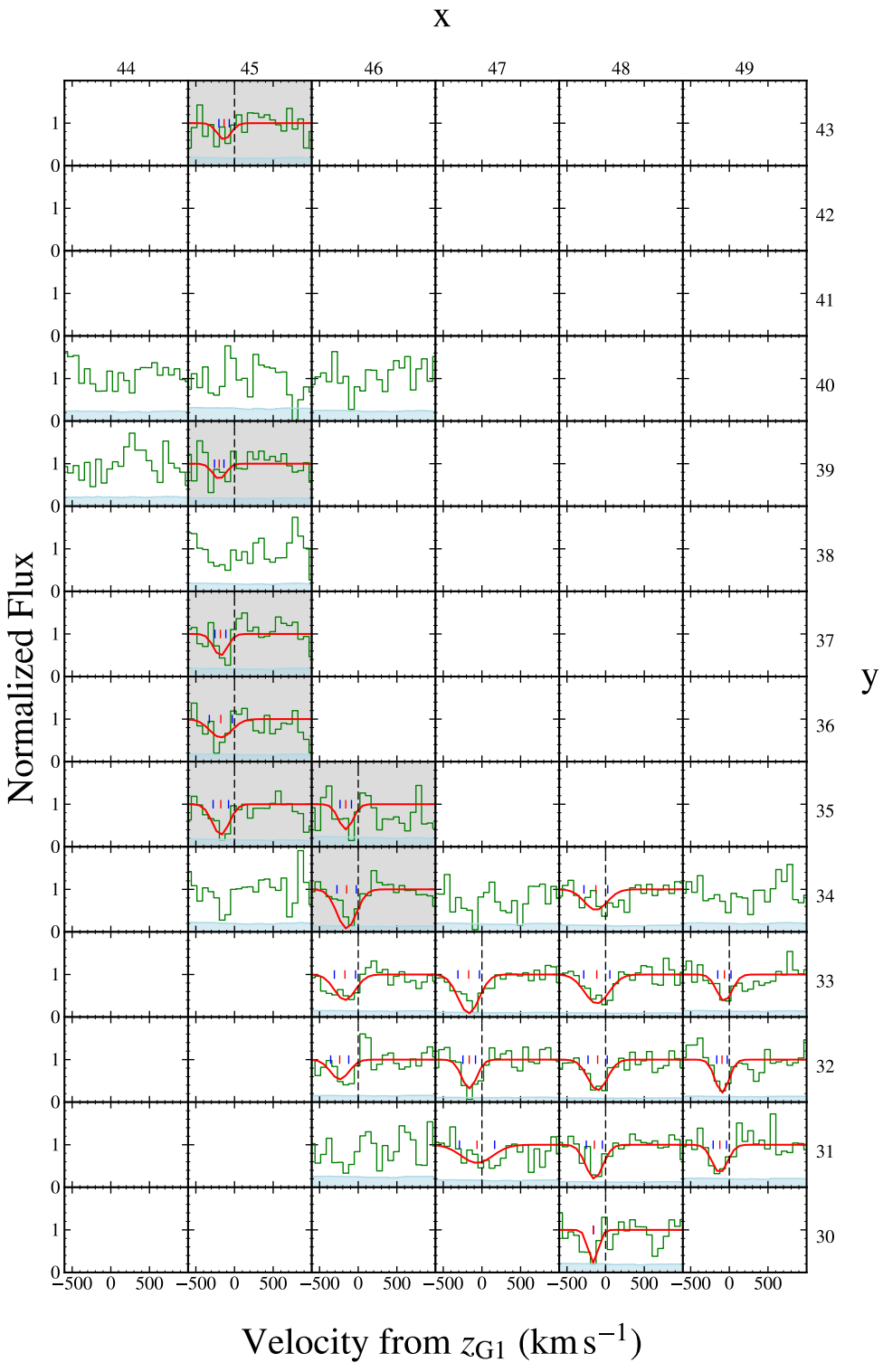

Fig. G.1. Same as Fig. F.1, but for the Fe II spectra. The dashed black vertical lines indicate the zero velocity of the Fe II λ2600Å transition at z_{G1}. The grey-shaded panels indicate transverse sightlines with detected Mg II absorption.